1

Satellite Observed Salinity Distributions at High Latitudes in the

Northern Hemisphere: A Comparison of Four Products

Cynthia Garcia-Eidell[1,2]

cynthia.o.garcia@nasa.gov

Josefino C. Comiso[1,5]

josefino.c.comiso@nasa.gov

Emmanuel Dinnat[1,3]

emmanuel.dinnat@nasa.gov

Ludovic Brucker[1,4]

ludovic.brucker@nasa.gov

[1]NASA Goddard Space Flight Center,

Cryospheric Sciences Laboratory, Greenbelt, MD 20771, USA

[2]Wyle Science Technology and Engineering,

2400 NASA Parkway, Houston, TX 77058, USA

[3]Center of Excellence in Earth Systems Modeling and Observation,

Chapman University, Orange, CA 92866, USA

[4]Universities Space Research Association, Goddard Earth Sciences Technology

and Research Studies and Investigations, Columbia, MD 21044, USA

[5]Corresponding Author

25 **Key Points:** 1. Satellite-derived sea surface salinity in the Arctic region from four products, three

26 from Aquarius and one from SMOS are compared.

27 2. Validation studies indicate good agreement of satellite data with in situ salinity measurements

28 and usefulness of the data in monitoring spatial and temporal variability in the Arctic.

29 3. Significant discrepancies in the spatial and temporal distribution are observed between the

30 products as a result of differences in noise reduction and smoothing and in the masking of land

31 and sea ice.

32 4. All products showed general consistency in capturing sea surface salinity's seasonality and

33 interannual variability in the Arctic if similar data quality control is applied.

34

35 **ABSTRACT**

36 Global surface ocean salinity measurements have been available since the launch of SMOS in

37 2009 and coverage was further enhanced with the launch of Aquarius in 2011. In the polar regions

38 where spatial and temporal changes in sea surface salinity (SSS) are deemed important, the data

39 has not been as robustly validated because of the paucity of in situ measurements. This study

40 presents a comparison of four SSS products in the ice-free Arctic region, three using Aquarius

41 data and one using SMOS data. The accuracy of each product is assessed through comparative

42 analysis with ship and other in situ measurements. Results indicate RMS errors ranging between

43 0.33 and 0.89 psu. Overall, the four products show generally good consistency in spatial

44 distribution with the Atlantic side being more saline than the Pacific side. A good agreement

45 between the ship and satellite measurements were also observed in the low salinity regions in the

46 Arctic Ocean, where SSS in situ measurements are usually sparse, at the end of summer melt

47 seasons. Some discrepancies including biases of about 1 psu between the products in spatial and

48   temporal distribution are observed. These are due in part to differences in retrieval techniques,

49   geophysical filtering, and sea ice and land masks. The monthly SSS retrievals in the Arctic from

50   2011 to 2015 showed variations (within ~1 psu) consistent with effects of sea ice seasonal cycles.

51   This study indicates that spaceborne observations capture the seasonality and interannual

52   variability of SSS in the Arctic with reasonably good accuracy.

53

54   **1. Introduction**

55   Salinity has been regarded as one of the key geophysical parameters that affect ocean circulation,

56   hydrological cycle, ocean ecology and changes in the climate. Together with temperature, it

57   drives the thermohaline circulation of the ocean, which influences the transport of heat, energy

58   and humidity thereby modulating climate [*Aagard et al.*, 1985; *Broecker,* 1997]. Salinity is also

59   an abiotic factor that shapes the ecological landscape of the environment and the distribution of

60   nutrients that are consumed by algae and other biological species in the ocean. It has also been

61   used as a tracer of water mass movement and advection characteristics of surface water [*Durack*

62   *et al.,* 2012]. Despite the importance of monitoring salinity, knowledge of its global distribution

63   and the variations of such distribution both in space and time has been inadequate. Ocean-mixing

64   processes and freshwater discharge mechanisms remain poorly understood notwithstanding

65   possible connections of warming with high-latitude freshening [*Schmitt,* 2008]. Such global

66   distributions are not expected to be spatially uniform on account of many factors. For example,

67   salinity is low in some areas because of the transport of freshwater through precipitation, river

68   runoff, and in higher latitudes, ice melt from sea ice and land ice [*Lehner et al.,* 2012; *Nummelin*

69   *et al.,* 2016]. It is also relatively higher in areas where there is excessive evaporation or sea ice

70   production.

71

72 The lack of in situ salinity data is an even more serious challenge in the Arctic region due to the

73 very sparse sampling partly due to the harsh environment, adverse weather conditions and the

74 presence of sea ice. Such limitations are unfortunate because large spatial and temporal

75 variabilities in sea surface salinity (SSS) are expected in the Arctic region because of the highly

76 seasonal sea ice cover and a summer ice minimum that has been observed to be changing rapidly

77 [*Vaughan et al.,* 2014*; Cavalieri and Parkinson,* 2012*; Comiso et al.,* 2008]. In addition, glacial

78 melt contribution from the Greenland ice sheet has been increasing significantly from 170 to 360

79 km^3/year [*Khan et al.,* 2014]. This mass loss is expected to significantly impact the thermohaline

80 circulation and as *Dukhovskoy et al.,* in 2016 estimates, surplus Greenland freshwater flux should

81 cause salinity decrease of 0.06-0.08 in the sub-Arctic seas. Such changes are expected to cause

82 variations in salinity and temperature distributions that could affect the circulation and

83 productivity of the Arctic Ocean and surrounding seas. The observed salinity anomalies in the

84 Arctic has also been linked to changes in the phase of the Arctic Oscillation [*Houssais et al.*,

85 2007].

86

87 Fortuitously, satellite L-band sensors (operating at a frequency of ~1.4 GHz) have been developed

88 in recent years and are well suited for monitoring global distributions of SSS at a reasonable

89 temporal resolution of about one week or longer. The earliest of these is the European Space

90 Agency's (ESA) Soil Moisture and Ocean Salinity (SMOS), which is a purely passive system

91 launched on 02 November 2009. The next one was the Aquarius SAC-D, launched on 10 June

92 2011, which was a joint venture of National Aeronautics and Space Administration's (NASA) and

93 Argentina's Comision Nacional de Actividades Espaciales (CONAE). Unfortunately, Aquarius

94   ceased operation on 07 June 2015 but NASA's SMAP (Soil Moisture Active Passive) was

95   launched on 31 January 2015. The latter is meant to measure soil moisture but also has the

96   capability of providing estimates of surface salinity. The important question is how accurately the

97   salinity distribution can be derived especially in the relatively cold high latitude waters where

98   retrieval techniques have the most problem.

99

100   The primary goal of this study is to evaluate and assess the accuracy of spatial and temporal

101   variabilities of the SSS in the Arctic region as derived from satellite data. To achieve this goal, a

102   comparative study is performed using four SSS products from Aquarius and SMOS at high

103   latitudes in the Northern Hemisphere. These products are compared with available ship

104   thermosalinograph (TSG) measurements and with quality-controlled CORA (COriolis Ocean

105   database for ReAnalysis) [*Szekely et al*, 2015; *Cabanes et al*, 2013] in situ dataset to establish

106   confidence about the validity of the techniques used in creating the products from the L-band

107   satellite observations. Through this process we assess the uncertainties associated with these

108   existing products to ensure proper interpretation of the results of analysis. Data from 2011 to

109   2015 are then analyzed to study the seasonal and yearly changes in the spatial distribution of SSS

110   during this period as consistently revealed by satellite data.

111

112   **2. Methodology and Satellite Data Products**

113   *2.1. Retrieval of SSS from Satellite Data*

114   Satellite passive microwave systems have been around since the 1970s but have not been used

115   until recently for salinity measurements because the systems did not have the low-frequency

116   requirement needed to be sensitive enough to measure SSS. The right wavelength and algorithms

117   are needed to remove ambiguities and be able to establish that the geophysical parameter that is

118   being measured is SSS. The ambiguities are associated with the influence of many other factors

119   such as sea surface temperature (SST), roughness, atmospheric conditions and others on the

120   brightness temperature of the surface. Although salinity can be derived through the sole use of

121   data from passive microwave radiometers, further improvements in accuracy is expected through

122   a combined passive and active system as will be discussed below.

123

124   The techniques for the retrieval of salinity from passive microwave data have been discussed in

125   many publications that includes the Algorithm Theoretical Basis Documents (ATBD) [e.g., *Le*

126   *Vine et al.*, 2011; *Brucker et al.*, 2014; *Wentz and Yueh*, 2011; *Wentz and Le Vine*, 2012; *Yueh et*

127   *al.*, 2014; *Meissner et al.*, 2014]. The physics of the techniques are basically the same and make

128   use of a radiative transfer forward model to retrieve the surface brightness temperature (T_B) from

129   Aquarius (and SMOS) measurements. The contaminations to the measured signal due to radiation

130   from the galaxy, sun, moon and Earth's atmosphere are estimated [*Dinnat and Le Vine*, 2008;

131   *Dinnat et al.*, 2009] and deducted from measured antenna temperatures (T_A). For the Aquarius

132   algorithm, an antenna pattern correction is applied to remove cross-polarization effects and

133   Faraday rotation is removed using the 2nd and 3rd Stokes parameters [*Yueh*, 2000; *Le Vine et al.*,

134   2013]. To correct for atmospheric contributions, National Centers for Environmental Prediction

135   (NCEP) profiles of temperature, pressure, liquid water and humidity were interpolated to the

136   location of Aquarius measurements. Reynolds OI SST product is used as the ancillary SST field.

137   After the corrections are applied, the resulting term is the brightness temperature of the ocean

138   surface, T_B that is used to obtain the surface salinity.

139

140 In the microwave frequency region, the Stefan-Boltzmann's Law reduces to Rayleigh-Jeans

141 approximation, which is given by the equation:

142 $$T_B = \epsilon * SST \tag{1}$$

143

144 where SST and ϵ are the temperature and emissivity of the surface, respectively. The emissivity

145 is the key radiative property of the surface and contains the information associated with salinity in

146 ocean-covered regions. The emissivity, which depends on incident angle, can be inferred from the

147 surface reflectivity (R) as:

148 $$\epsilon = 1 - R \tag{2}$$

149

150 with R a function of the surface roughness, incidence angle and sea water dielectric constant, ε,

151 which depends on SST, SSS and radio frequency.

152

153 All algorithms have to account for the impact of surface roughness in order to retrieve SSS, see

154 examples in [*Meissner et al.,* 2014; *Yueh et al., 2014*]. Aquarius makes use of its active

155 measurements from its collocated radar scatterometer to improve the surface roughness

156 correction, which is an asset that neither SMOS nor SMAP have (SMAP's radar failed three

157 months into the mission in July 2015). Remote sensing theory and airborne experiments have

158 demonstrated the importance of the radar in providing complementary information about the wind

159 and surface roughness for L-band remote sensing [*Yueh et al.*, 2001; *Yueh et al.*, 2010; *Martin et*

160 *al.*, 2014] and uncertainty on Aquarius SSS retrievals is significantly reduced with the inclusion

161 of radar observations (see Table 3 in *Meissner et al.*, 2014).

162

163   It is apparent that the retrieval of SSS requires the knowledge of many parameters some of which

164   need to be estimated through models or special techniques. The models and techniques are not as

165   well validated in the Arctic as in other regions because of the paucity of data as illustrated in the

166   map shown in Figure 1a. The map shows data points from Argo buoys (in blue) and other in situ

167   data sources (in red) and indicates that the locations of most of the in-situ data are primarily in the

168   subarctic regions while there is hardly any data north of 60°N. The map also serves as a location

169   map that indicates where the various seas in the region are located as well as the mouth of key

170   rivers where significant amounts of fresh water are introduced to the Arctic Basin.

171

172   The dependence of T_B at 1.4 GHz (L-band) and 35° incidence angle on SST for different values

173   of SSS from 25 psu to 29 psu are illustrated in Figure 1b and 1c for vertical and horizontal

174   polarizations, respectively. The relatively low sensitivity of SSS at low temperature waters

175   compared to those in warmer waters are apparent making the ability to obtain accurate salinity a

176   bigger challenge in the Arctic (i.e., cold) region than in lower latitude regions. The two plots also

177   show that at a given temperature, T_B decreases as SSS increases. It can be seen that the SSS

178   spread is wider in the vertical component than in the horizontal component, thus, making the

179   former slightly more sensitive to SSS changes. In addition to this, *Brucker, et al.*, [2014] and

180   *Dinnat and Brucker,* [2017] showed that T_B is also highly sensitive to the presence of sea ice due

181   to the differences in emissivity, which can be interpreted as an erroneous decrease of SSS or

182   freshening.

183

184   *2.2. Data Source and Data Products*

185 The key sources of satellite data that are currently used for the retrieval of SSS are Aquarius and

186 SMOS sensors. Recent launch of SMAP provides a third source but since advanced processing is

187 still in progress, SSS data are not yet publicly available at the time of this study and therefore only

188 data from Aquarius and SMOS were used.

189

190 The Aquarius satellite is composed of three radiometers and one scatterometer operating at L-

191 band. The radiometers operate at 1.414 GHz and their beams have incidence angles of 29.2°,

192 38.48° and 46.3°, providing us with a total cross track of 370 km and footprints of 74 km x 94

193 km, 84 km x 120 km, and 96 km x 156 km, respectively. Aquarius' scatterometer operates at 1.26

194 GHz and is primarily used to account for surface roughness correction in the salinity retrievals.

195 With a swath width of 390 km global coverage by Aquarius is achieved in seven days but since

196 the satellite is polar orbiting with an inclination angle of 98° there is more coverage in the polar

197 regions and our domain is completely covered every 3 days. The mission's required accuracy is

198 0.2 psu after averaging over a month at a resolution of 150 km x 150 km in global open oceans.

199 This study made use of three Aquarius SSS products, namely: (1) Aquarius level-2 official release

200 product (V4.0), [*Meissner et al.*, 2014]; (2) Aquarius level-2 CAP product (V4.0), [*Yueh et al.*,

201 2014]; and (3) Aquarius level-3 Weekly polar-gridded product (V5.0), [*Brucker et al.,* 2014].

202

203 The ESA/SMOS satellite has only one sensor - a passive system called Microwave Imaging

204 Radiometer using Aperture Synthesis (MIRAS) also operating at L-band. It has a tilt angle of

205 32.5° and spatial resolution of 35 km at center of field of view. The range of incidence angles

206 varies from 0 to about 40 degrees over the field-of-view and the resolution changes with the angle

207 of incidence. Total global coverage is achieved by SMOS in three days while the entire study

208 domain is covered every two days. The mission required accuracy is 0.1 psu when data is

209 averaged over a month on a 200-km scale [*Berger et al.,* 2002]. For this study, the Barcelona

210 Expert Centre (BEC) SMOS level-3 Experimental product at high latitude ocean areas was used

211 [*Gabarro et al.,* 2016]

212

213 Although they have the same goal of monitoring SSS using L-band observations, SMOS and

214 Aquarius differ in both instrument design and SSS derivation approach. Aquarius has both

215 radiometer and scatterometer, which helps in correcting for sea surface roughness. SMOS spatial

216 resolution is finer than Aquarius' and also has shorter time of revisit. *Dinnat et al,* [2014b]

217 compared SMOS and Aquarius SSS and observed that SMOS SSS values are generally lower

218 than Aquarius SSS, except in cold waters. They also pointed out the difference between the

219 forward models used; ancillary data utilized as input to the model, and the calibration parameters.

220 SMOS uses the *Klein and Swift* [1977], while Aquarius uses the *Meissner and Wentz* [2012]

221 dielectric constant model. The ancillary SSS used by SMOS for the forward model is the World

222 Ocean Atlas 2009, [*Boyer et al.,* 2009]*,* while Aquarius uses the Hybrid Coordinate Ocean Model

223 (HYCOM), [*Chassignet et al.,* 2007]. Calibration was also done over a region in the Pacific

224 Ocean for SMOS while for Aquarius it is done globally. Details of the SSS gridded data products

225 used in this study are presented in the following sections.

226

227 *2.2.1. AqGSFC: Aquarius level-2 official release product (V4.0)*

228 Produced by NASA Goddard Space Flight Center's Aquarius Data Processing System (ADPS),

229 Aquarius level-2 product contains retrieved orbital/swath SSS, wind speed from both radiometers

230 and scatterometer, brightness temperature at V and H polarization, quality flags, converted

231   telemetry, navigation data and ancillary data from select sources. In this study, we use the latest

232   version (V4.0) which provides estimates of density and SSS-uncertainty variables and have the

233   SST-dependent bias correction implemented directly into the baseline algorithm. Significant wave

234   height (SWH) for surface roughness correction was also included along with tuning of parameters

235   of the RFI filter over land. More details on the improvements made from V3.0 to V4.0 are in the

236   dataset validation analysis done by *Lagerloef et al.* [2015] and accompanying Addendum to the

237   ATBD by *Meissner et al.* [2015]. Dataset and user guide were downloaded from NASA's

238   Physical Oceanography Distributed Active Archive Center (PO.DAAC),

239   ftp://podaac.jpl.nasa.gov/SalinityDensity/aquarius/.

240

241   In this study, the SSS gridded product called AqGSFC, was generated using the level-2

242   orbital/swath official release data.   The data were first geophysically filtered in a given grid point

243   by discarding retrieved salinity with land fraction greater than 0.01, sea ice concentration greater

244   than 0.01 and wind speed greater than 20 m/s. Wind speed greater than 20 m/s causes surface

245   roughness that requires a special correction. Data with the following contamination flags (and

246   flag number) were also removed from the gridded product: unusual brightness temperature (flag

247   #6); direct solar flux contamination (#7); reflected solar flux contamination (#8); sun glint (#21);

248   non-nominal navigation (#12); pointing anomaly (#16); brightness temperature consistency (#17);

249   RFI contamination (#19) and Moon and Galactic reflected contamination (#21). Salinity

250   measurements more than 40 psu or less than 20 psu were not included. To further remove data

251   points potentially contaminated by presence of sea ice, Bootstrap Sea Ice Concentration (SIC)

252   data from the Special Sensor Microwave/Imager (SSM/I) and Special Sensor Microwave

253   Imager/Sounder (SSMIS), also known as the SB2 product [*Comiso et al.,* 2017] was used to mask

254   out SSS readings with SIC greater than 15%. This was performed as the existing ice fraction

255   derived from Aquarius brightness temperature tends to overestimate sea ice fraction in the

256   marginal ice zone [*Dinnat and Brucker,* 2017]. The ice edge as inferred from SSM/I has been

257   validated to be reasonably accurate even during the meltponding season [Comiso and Nishio,

258   2008].

259

260   Both ascending and descending orbits from all three beams were used in the processing. Each

261   beam was filtered to suppress the noise along track, which was earlier suggested by *Melnichenko*

262   *et al.* [2014] as a necessary step to improve accuracy of individual measurements along the track.

263   Figure 2 shows the three beams (dotted line) passing through North Atlantic (Ascending) and

264   North Pacific (Descending) starting at 6:12 PM UTC on 02 July 2012. The solid curves in Figures

265   2a and 2b are the result after the initial geophysical filtering and subsequent smoothing with a

266   median filter with window of 9 observations. Aquarius data block period is every 1.44 seconds. It

267   can be seen that random short-wavelength noise along track per beam was effectively suppressed.

268   Another issue is the differences between the three beams due to the slightly varied view of the

269   ocean surface. Since the beams are with different incidence angles, the geophysical errors to be

270   observed per beam are expected to be different [*Lagerloef et al.,* 2013]. Along with the

271   geophysical filtering performed in the initial phase of processing, taking into account only severe

272   conditions, we also tried to minimize the effect of inter-beam biases by performing bilinear

273   interpolation in between beams. Given that the Aquarius SSS data are spatially inhomogeneous, a

274   median filter was used to remove noise while preserving edges and important details in the data.

275   Median filter is also effective in removing random noise (isolated high or low values) and

276   requires much less processing time than removal by frequency domain Fourier transforms

277   [*Nichols, et al.*, 2004]. Level-2 orbital/swath files were gridded on to the polar stereographic grid

278   with 12.5 km resolution. This resolution was chosen because Aquarius has an along-track

279   sampling of an observation every 10 km, thus, offering a refined spatial resolution. Running

280   weekly maps were produced corresponding to the satellite's time of revisit for years 2011 to

281   2015. The location of the ice edge was also indicated by including a contour of the SB2 SIC edge

282   in the SSS maps.

283

284   *2.2.2. AqJPL: Aquarius Level-2 Combined Active-Passive (CAP) product (V4.0)*

285   The level-2 CAP SSS and wind speed are calculated using the updated CAP retrieval algorithm

286   [*Yueh et al.,* 2014] from Aquarius T_B and scatterometer backscatter by minimizing the sum of

287   squared differences between model and observations. Aside from the CAP algorithm outputs, the

288   product also includes flags for valid data and data with possible rain contamination using match-

289   ups based on NOAA Climate Prediction Center morphing method (CMORPH) half-hourly global

290   precipitation estimates at 0.25° resolution. It is distributed through NASA's Physical

291   Oceanography Distributed Active Archive Center (PO.DAAC) 's homepage,

292   ftp://podaac.jpl.nasa.gov/SalinityDensity/aquarius/.

293

294   The SSS product as described above and called AqJPL also has rain correction and was gridded in

295   the same projection, spatial and temporal resolution, and filtering techniques as that with the

296   AqGSFC product. Observations with CAP flags ≥ 3 or ≤ 9 and ≥ 13 were discarded. More details

297   on the Level-2 CAP flags are provided in the Aquarius CAP Algorithm and Data User Guide

298   V4.0 [*Yueh et al.,* 2015]. SSS retrievals with land and ice fraction greater than 0.01, flagged with

299   non-nominal navigation, and pointing anomaly were not included. Salinity measurements more

300   than 40 psu or less than 20 psu were also discarded

301

302   *2.2.3. AqNSIDC: Aquarius Level-3 weekly polar-gridded product (V5.0)*

303   Level-3 weekly polar-gridded product (V5.0) by *Brucker, et al.* [2014], distributed by the US

304   National Snow and Ice Data Center at http://nsidc.org/data/aquarius/index.html) was also

305   processed from level-2 orbital/swath product and includes SSS at latitudes higher than 50°. Data

306   set consists of the average SSS retrieved from all three Aquarius radiometers, gridded to the

307   EASE2.0 grid with 36 km resolution. Interpolation was done using Delaunay triangulation. In

308   this paper, for ease of comparison, this product, referred to as AqNSIDC, was regridded in the

309   polar stereographic grid at 12.5 km resolution. Same smoothing technique was also applied as

310   those used for the AqGSFC and AqJPL.

311

312   *2.2.4. SmosBEC: SMOS-BEC Experimental product in high latitude ocean areas*

313   Distributed by the Barcelona Expert Center (BEC) at http://cp34-bec.cmima.csic.es., the

314   objectively analyzed high latitude SMOS SSS product was gridded on to the EASE grid at 25km

315   resolution, averaged every nine days. The data, referred to as SmosBEC, is available for years

316   2011 to 2013 only. BEC processed the SMOS level-2 data by discarding salinity measurements

317   with galactic, sun glint and surface roughness contamination. For this experimental product, BEC

318   used the *Meissner and Wentz* dielectric constant model in the computation of SSS. The individual

319   SSS measurements were subtracted from the computed SMOS climatological value to get an

320   anomaly product. Annual objectively analyzed SSS climatological field (WOA13 V2.0) was

321   added to the SMOS anomaly product to compute for the absolute value of SSS.

322

3. Comparative Studies and Error Analysis

324 Salinity data obtained from a research vessel and quality-controlled CORA (COriolis Ocean

325 database for ReAnalysis) in situ dataset provided the key validation measurements used for

326 comparative studies and for estimating the accuracy of satellite SSS data. A number of validation

327 studies were conducted previously but done mostly in low latitude warm waters. For example,

328 *Ebuchi* and *Abe* [2014] made use of Argo data in tropical areas and found a systematic negative

329 bias in the satellite measurements, which they attributed to near-surface salinity stratification due

330 to precipitation. Validation of Aquarius SSS data with moored buoys and Argo floats were also

331 done by Tang, *et al.* [2014] and determined that between 40°S and 40°N there is a strong

332 agreement between monthly Aquarius SSS and Argo measurements, except in the Eastern Pacific

333 Fresh Pool and Amazon River outflow. Similarly, *Boutin et al.* [2013] showed that SMOS SSS

334 agree well with Argo measurements with standard deviations of 0.35 in the Tropical Pacific

335 Ocean and 0.28 in the Subtropical Atlantic Ocean and that the values correlate well with the

336 freshening associated with precipitation as derived from SSMI rain in the Intertropical

337 Convergence Zone of the Pacific. Also, *Banks et al.* [2012] found that the SMOS SSS products

338 generally agree with Argo floats and ocean model simulations in the Atlantic Ocean except in

339 coastal regions.

340

341 Despite the importance of having good SSS satellite retrievals at high latitudes, only a few SSS

342 validation studies have been conducted so far in the region. The aforementioned decrease in SSS

343 sensitivity with decreasing sea surface temperature (SST) has been reported by *Lagerloef et al.*

344 [2015] but the overall quality of SSS in the Arctic has not been assessed. Also, significant

345 instrument noise and large-scale satellite biases have been observed in the region [*Melnichenko et*

346 *al.*, 2014]. In connection to this, *Kohler et al.* [2014] studied SST-related biases in both Aquarius

347 and SMOS SSS products through their validation in the northern North Atlantic using ship-based

348 TSG and Argo data. *Brucker et al.,* [2014] and *Dinnat and Brucker,* [2017] indicated that a key

349 source of error in the retrieval of SSS from Aquarius in the polar oceans has been land and sea ice

350 contaminations. Sea ice and land masks derived from satellite data are available to minimize this

351 problem but the implementation of these masks by the different SSS products is different. Other

352 potential sources of error are the uncertainty on SST and the sea water dielectric constant model

353 [*Dinnat et al.,* 2014a].

354

355 *3.1. Comparison with Thermosalinograph Data from Icebreakers*

356 Collected in situ salinity data from PFS Polarstern with cruise IDs: ARK27-1, ARK27-2, and

357 ARK27-3 from 15 June to 06 October, 2012 and ANT28-3, ANT28-4, and ANT28-5 from 08

358 June to 04 October, 2014, covering Nordic Seas and the Arctic Ocean were used to validate the

359 satellite-derived gridded SSS products. Only TSG measurements with quality flag equal to 1

360 (good) were used for this study. However, there is a possibility that the TSG measurement might

361 represent a perturbed version of the surface that might cause mismatches with the satellite

362 measurements. Figure 3 shows color-coded tracks of the ship to indicate salinity values observed

363 along the tracks and location of comparative studies. The contour of the SB2 sea ice concentration

364 product during each year's minima was also applied to indicate the location of the sea ice edge.

365 Two sensors installed in the ship's bow and keel measured salinity of the seawater. Both are

366 regularly calibrated with accuracy of <0.01. Data were downloaded from

367 http://cdiac.ornl.gov/ftp/oceans/VOS_Polarstern/.

368

369 It is clearly seen in Figure 3 that the spatial distribution of the ship SSS measurements appears to

370 be generally consistent with the presence of low surface salinities in the Arctic Ocean and

371 bordering seas, likely associated with the melt of sea ice and river run-off during the June to

372 October period for both 2012 and 2014.

373

374 Direct comparison of Polarstern SSS and the different satellite derived SSS products as discussed

375 earlier are presented in Figure 4a to 4d. The plots are color-coded to show differences in the SSS

376 values for different time periods and locations during the 2012 campaign as indicated as transect

377 A to D in Figure 3a. The in situ Polarstern data have much larger spatio-temporal variability than

378 the remote sensing products in part because the sampling is much more frequent than those of the

379 satellite data sets (e.g. sampled every minute compared to multi-day averages) and the satellite

380 sensor footprints are much larger than single point ship observations. Aquarius has three

381 ellipsoidal footprints of 74 km x 94 km, 84 km x 120 km, and 96 km x 156 km, while SMOS has

382 a footprint of 40 km. The discrepancies between the different products are sometimes quite large

383 and in some places greater than 1 psu with SmosBEC appearing to be the one most consistent

384 with Polarstern except in Figure 4b, where the ship measured SSS as low as 25 psu, which were

385 effectively captured by the Aquarius products. The values usually fall between 34 and 36 psu,

386 except in Figure 4b where the salinities are much lower and between 25 to 32 psu as expected in

387 the Central Arctic during this time period because of the melt of sea ice and river runoffs.

388

389 Scatter plots showing more direct comparison of the different satellite products with Polarstern

390 data are presented in Figure 4e to 4h. The results are similar for the different products with the

391   AqGSFC having the lowest standard deviation of 0.47 psu while AqJPL has the highest at 0.55

392   psu. Also, SmosBEC has the lowest RMS error of 0.51 psu while AqNSIDC has the highest at

393   0.69 psu. The correlation coefficients are all high, averaging 0.97, indicating good general

394   agreement of satellite with in situ data.

395

396   The AqNSIDC product [*Brucker et al., 2014*] has larger RMS error in part because it allows for

397   larger sea ice fractions in the product, which also keeps lower SSS values in the maps (down to ~

398   25 psu). It is a compromise between letting the error grow and removing some features near the

399   ice edge. The product was designed this way to let the user apply their best judgment for the given

400   application; here all available values were used.

401

402   Similar plots but for data in 2014 are presented in Figure 5. SmosBEC data has not been

403   processed for 2014 and later years and therefore missing in the comparative study. The plots

404   show that Polarstern data agree best with AqNSIDC in Transect E (Figure 5a) while they agree

405   best with AqGSFC and AqJPL in Transect F (Figure 5b). In Figure 5c, AqGSFC and some

406   AqNSIDC measurements were able to follow the low salinity readings of the ship, with SSS

407   ranging from 33 to 25 psu measured in the Arctic Ocean at the end of summer and early autumn

408   (see Figure 3b). AqJPL did not have SSS data on this segment perhaps because of inaccurate

409   masking of sea ice as well as the stringent parameters used in the CAP flags relative to wind

410   speed and possible rain contamination. In addition, AqGSFC and AqJPL appear to be more

411   consistent with each other. The large difference between the AqNSIDC with the other Aquarius

412   products is unexpected and could be attributed to the along-track filtering performed on AqGSFC

413   and AqJPL to get rid of random short-wavelength noise per beam. AqNSIDC product is also

414   available as a weekly average and not on a running weekly average, which can slightly affect the

415   accuracy of each collocation, centered on the ship's observation date.

416

417   Although the scatter plots show general agreement with high correlations, some biases are still

418   observed and can also be a result of short time scale surface mixing as indicated earlier or other

419   processes. Table 1 summarizes the computed average biases, RMS errors and correlation

420   coefficient values for years 2012 and 2014.

421

422   *3.2. Comparison with CORA v5.0.*

423   Another source of in situ data that can be used for validation studies is the Coriolis Ocean Dataset

424   for Reanalysis Dataset (CORA). The latest publicly available version of the product is called

425   CORA5.0, which provides a collection of existing in situ measurements of salinity on a global

426   scale to up to year 2015. The data are aggregated from different instruments such as Argo floats,

427   XBT, CTD, XCTD, French RV TSG measurements, Sea Mammals, Surface Drifters and

428   Moorings, and are received and stored in the Coriolis database in collaboration with the In Situ

429   Thematic Centre of the Copernicus Marine Service (CMEMS INSTAC). CORA measurements

430   undergo various quality checks and objective analysis to guarantee spatial and temporal

431   consistency. Detailed information on the product is available at:

432   http://marine.copernicus.eu/documents/PUM/CMEMS-INS-PUM-013-001-b.pdf.

433   Data can be downloaded at: http://www.seanoe.org/data/00351/46219/.

434

435   In this study, geographically and daily surface data, starting 26 August 2011 to 06 June 2015 with

436   quality index 1 – 4 (good to acceptable) were used and mapped to the same grid format as in the

437   other data sets. The data accumulated for said dates are presented in Figure 6a and it is apparent

438   that the data coverage is relatively sparse. However, the spatial distribution of SSS as depicted

439   appears to be generally consistent with satellite data. For quantitative comparison with the

440   satellite SSS products, scatter plots of CORA5.0 SSS data versus those of the four products are

441   shown in Figures 6b, 6c, 6d and 6e. The scatter plots show relatively good agreement in most

442   points in all products. Regression analysis was done on each set of products with CORA5.0 (blue)

443   and on datasets common among all the products with CORA5.0 (red) to remove the impact of the

444   differences in coverage between the products. Outliers are also filtered out. It is interesting to note

445   that there are two distinct clusters, especially when considering data common among products,

446   with the upper one corresponding to the data measured from the Atlantic and the lower one for

447   data in the Pacific. The clusters indicate that the two oceans are in different salinity regimes with

448   the range of values indicated in the clusters. When all data available for each product are used,

449   the correlation coefficients are 0.913, 0.906, 0.898, and 0.944 for AqGSFC, AqJPL, AqNSIDC

450   and SmosBEC, respectively. When only data points common to all four satellite products are

451   used, the corresponding values are 0.921, 0.920, 0.898 and 0.943. This shows that the lower

452   correlation coefficient of Aquarius products in the first set, in particular for AqNSIDC, is in part

453   due to more data being available in challenging areas such as near land and ice. The RMS errors

454   considering all common measurements are 0.412, 0.487, 0.465 and 0.323, which are much better

455   that those derived from the comparative analysis using Polarstern data. The actual error in the

456   satellite data is likely smaller since the CORA5.0 data set is not perfect as indicated above and

457   there are uncertainties in the matching of in situ with satellite data. Overall, the results indicate

458   that the data is promising with the correlation coefficients being quite high and the RMS errors

459   relatively low.

460

4. Results of Analysis

4.1 Comparison of Spatial Distribution for Different SSS Products

Typical SSS distributions in the Arctic region as derived from the different products during spring

and early autumn are presented in Figures 7 and 8. Figures 7a through 7d shows weekly averages

for the period 31 May to 6 June using AqGSFC and AqJPL data and the period 31 May to 7 June

for AqNSIDC and 31 May to 7 June for SmosBEC data. For convenience in the comparative

analysis, the different products are mapped in the same format and covering the same general

area. Note that the high latitude AqNSIDC and SmosBEC products cover greater than 50°N and

45°N only, respectively, while the AqGSFC and AqJPL products which are both derived from

level 2 products provide data for the entire mapping region. In the comparative analysis, we show

differences between data sets where there is overlapping data. The slight differences in dates are

caused by differences in the dates of the original products but should be a minor issue in the

qualitative comparison.

The spatial distribution of the different products shows similar general characteristics. For

example, the salinities in the Northern Pacific Ocean are generally lower than those in the

Northern Atlantic Ocean as mentioned earlier. This is consistent with more precipitation than

evaporation in the Pacific Ocean and vice versa in the Atlantic Ocean [*Broecker, 1997*]. Also,

salinities at lower latitudes are generally higher than those at higher latitudes. The salinity

distributions are most similar for AqGSFC and AqJPL as would be expected since they are

derived from the same level 2 Aquarius data set but with different retrieval algorithms.

AqNSIDC (Figure 7c) shows the smoothened version of the product, which effectively removed

483   the striped noise caused by the push-broom configuration of the Aquarius sensor as well as

484   minimized the effect of the unique sampling pattern of Aquarius satellite, where two or even three

485   beams coincide [*Lilly et al.,*2008]. Figure 7d shows basically the same pattern as the other three

486   Aquarius products but the SmosBEC product seems to display more noticeable differences

487   especially in the Bering Sea and freshening close to the mouth of Amur River in the Okhotsk Sea.

488   The differences are better quantified in Figures 7e, 7f, 7g and 7h, with the largest discrepancies

489   observed in the seasonal ice region (e.g., Okhotsk Sea) and likely associated with the presence of

490   sea ice.

491

492   The maps presented in Figure 8 are similar to those in Figure 7 but for the end of the summer to

493   early autumn and early autumn when the sea ice cover usually reaches its minimum. It is the time

494   period when the Arctic Basin has the least ice cover and more open water areas exposed to

495   satellite salinity measurements. Again, the maps shown in Figures 8a, 8b and 8c are generally

496   consistent but the coverage differs depending on the way the sea ice cover is masked from the

497   data. In this case AqNSIDC shows the least ice-related gaps due to the higher threshold of the

498   mask (Fig. 8c) while AqJPL shows more gaps than actually depicted in ice maps measured by

499   passive microwave sensors (i.e., see ice edge indicated by the red contour). All data products

500   show significantly lower salinity inside the Arctic basin than other areas. SmosBEC data show the

501   relatively low salinity close to river mouths as expected due to river runoff but little coverage in

502   the Arctic Basin because of poor sea ice masking (see Figure 8d). The difference maps presented

503   in Figures 8e to 8f shows a generally higher SSS in the AqJPL than the AqGSFC and AqNSIDC

504   products. The SmosBEC shows comparable but mainly lower values than AqGSFC except in the

505   South Atlantic Ocean region. Some anomalously high discrepancies are apparent in the Arctic

506   Basin that are likely mainly associated with contamination of the data by sea ice.

507

508   As previously observed in the SSS maps during spring, SmosBEC (Figure 8g and 8h) retrieved

509   more pronounced SSS variations close to the mouth of major Arctic rivers emptying into the

510   Arctic basin. The plume of Amur River (see Figure 1) flowing to the Sea of Okhotsk, measures up

511   to 2-3 psu lower than that of both AqGSFC and AqJPL. By the end of summer, lower SSS in the

512   river plumes of Kolyma, Ob and Mackenzie rivers can also be observed in the SmosBEC map.

513   However, AqGSFC, AqJPL and AqNSIDC showed more pronounced freshening in Beaufort Sea

514   as well as close to the mouth of Lena River, emptying into Laptev Sea. This supports the

515   validation findings using ship data, (as shown in Figures 4b and 4h) where SmosBEC got higher

516   SSS measurements (~3-4 psu) when compared to ship TSG measurements. In addition, AqNSIDC

517   and SmosBEC (other products not available) differ significantly in their depiction of the Kara Sea

518   river plume at the early autumn of 2012. SmosBEC shows a central propagation while AqNSIDC

519   shows an Eastern propagation, with the plume being pressed toward the Siberian coast. Analysis

520   by *Kubryakov et al.* [2016] suggests that in 2012 the river plume was propagating eastward. The

521   SmosBEC pattern may have been distorted by the calibration to the climatology, the Eastern

522   propagation of the plume being an unusual occurrence.

523

524   In the Atlantic Ocean region, Aquarius products as compared to the SmosBEC product best

525   captured the freshening caused by the melting of sea ice along the coasts of Greenland as well as

526   the melt of glaciers and the Greenland ice sheet *[Khan et al, 2014; Dukhovskoy et al, 2016]*. The

527   flow of fresh water from Davis Strait and Labrador Sea to the North Atlantic Ocean is also shown

528   to be pronounced in the Aquarius products in the early autumn. The export of low salinity polar

529   water to the North Atlantic is expected to affect the freshwater balance in the Arctic Ocean and

530   can have significant impact on the global climate *[Rudels,* 2011].   In comparing AqJPL and

531   AqGSFC, it can be seen that in general, AqJPL measured relatively higher salinity in early

532   autumn and relatively lower in spring.

533

534   *4.2. Interannual Variations in Salinity Distributions During Spring and Early Autumn*

535   The interannual changes in sea surface salinity have been quantified for the time period Aquarius

536   SSS data are available. Interannual changes are important to monitor because reports indicate that

537   SSS has been getting saltier in the Northern Atlantic while it is getting fresher in the Northern

538   Pacific *[Gordon and Giulivi, 2008].* Salinity maps for spring and early autumn are presented in

539   Figures 9 and 10, respectively. The spatial distribution of salinity in spring as described for 2012

540   in the previous section is also true for the other years as depicted in Figure 9. The yearly

541   differences are mainly in the seasonal regions and are most apparent in AqGSFC and AqJPL since

542   these maps show data at lower latitudes. The changes are most evident in the Pacific Ocean

543   where the 33 psu contour (in black) shows significant interannual variability. Note that the

544   patterns of interannual changes from the different products are similar despite significant

545   differences of the different products and especially those for AqGSFC and AqJPL which covers

546   the entire study areas.   The observed interannual changes are likely associated with interannual

547   changes in ice cover, ice dynamics and precipitation as maybe influenced by ENSO and the

548   Pacific Decadal Oscillation.   Since the differences between the four products are due to different

549   processing and noise reduction techniques the latter can be made more uniform to minimize the

550   differences. Subtler changes in SSS are observed in the Atlantic Ocean.

551

552 In early autumn, Figure 10 shows that interannual changes are apparent in all four products. In the

553 Pacific Ocean, significant interannual changes are evident especially in the Bering Sea and the

554 Okhotsk Sea. For example, SSS in parts of the Bering Sea in 2011 is almost 1 psu lower than the

555 SSS in 2014 in the three Aquarius products. Also, SSS in the Okhotsk Sea is lower in 2013 than

556 those of the other years. In the Arctic basin, the interannual differences are mainly due to yearly

557 change in the Arctic sea ice cover. Large differences in the masking of the sea ice cover (and also

558 land) are apparent for the different products making salinity data from these products less uniform

559 in the Arctic basin.

560

561 The changes in Kara Sea's plume distribution, particularly its westward extension was shown to

562 vary from year to year depending on wind regime [*Kubryakov et al.*, 2016]. This can be observed

563 in the AqNSIDC and SmosBEC products due to their extended coverage, which included more

564 data closer to the coast. SmosBEC shows changes in the extent of fresh water from the rivers

565 plume, while AqNSIDC shows changes both in extent and in shape of the plume. A possible salt

566 water intrusions from the Pacific Ocean through the Bering strait is also apparent in the Aquarius

567 products where some elevated SSS values at the Chukchi Sea are depicted. Such phenomenon

568 has been reported previously by [Coachman and Barnes, 1961]. The intruding Bering Sea water

569 separates deeper Atlantic water from the surface water in the Arctic and limits the depth of

570 vertical convection associated with the freezing of ice.

571

572 The results of quantitative assessment of the differences of the various products are presented in

573 Figure 11. Figures 11a and 11b shows monthly changes in salinity from 2011 through 2015 for

574   the Northern Pacific and Northern Atlantic Oceans areas, respectively. In the Northern Pacific

575   Ocean there appears to be a general agreement with the AqGSFC showing the most consistent

576   seasonality while SmosBEC shows the least seasonality and most discrepancy from the others.

577   This is possibly due to the use of climatological data to debias the SMOS retrievals. In the

578   Northern Atlantic Ocean, the discrepancies between the products are more significant and biases

579   between the different Aquarius products are more apparent.

580

581   Figures 11c and 11d show plots of SSS data > 65°N in both Western and Eastern Arctic Basin. It

582   is remarkable that the four SSS products agree so well in the region. In the Western Arctic Basin,

583   there is a good general agreement in the average values > 65°N with the monthly and interannual

584   changes associated with the changes in the sea ice cover. For convenience, the sea ice

585   concentration is plotted as a dash line to be able to assess the effect of sea ice melt. The lowest

586   average salinity values are indeed observed in early autumn 2012 when the extent of sea ice was a

587   record low and significant areas of open water are exposed. However, in Figure 11c, SmosBEC

588   show significantly higher SSS during the early autumn of 2012 than the other three products.

589   Improper masking of the sea ice cover as can be seen in Figure 10 causes this. In Figure 11d, the

590   AqJPL data does not show the drop in SSS during the early autumn of 2014. Again, this is caused

591   by improper masking of sea ice in the Arctic Basin. The good agreement of the three products

592   does not necessarily indicate good accuracy since the Arctic Basin is an area where the

593   uncertainties in the retrieval is supposed to be greater because of colder temperatures. There

594   could be a bias in the retrieved data that is currently not easy to detect due to the paucity of in situ

595   observations.

596

597 **5. Discussion and Conclusions**

598 The spatial and temporal distributions of SSS at high latitudes are studied through comparative

599 analysis of four different surface salinity products derived from L-band observations and ancillary

600 data. The four products include three from Aquarius as processed by different groups and one

601 from SMOS. The accuracy of each product is assessed through regression and correlation

602 analysis with quality-controlled ship measurements and CORA5.0 data set. The RMS errors

603 when compared with CORA5.0 data are 0.412, 0.487, 0.465 and 0.323 psu for the AqGSFC,

604 AqJPL, AqNSIDC and SmosBEC products, respectively. The RMS errors are very similar with

605 SmosBEC having a slight advantage in accuracy. The actual accuracy could be better since the

606 CORA5.0 data used in the analysis are not perfect and there are also errors in the matching of the

607 in-situ with the satellite products (e.g., footprint and ocean depth). Also, it is important to note

608 that the instruments were built to have a precision of about 0.2 psu. The RMS errors using

609 ship/Polarstern data in the Arctic region are higher at 0.515, 0.585, 0.686 and 0.507 psu for the

610 AqGSFC, AqJPL, AqNSIDC and SmosBEC products in 2012 and 0.806, 0.838, and 0.886 psu for

611 AqGSFC, AqJPL and AqNSIDC in 2014. The higher RMS errors when using ship data are likely

612 associated in part with the difficulty of matching ship measurements with satellite measurements.

613 The SmosBEC product is again more consistent than the other products in 2012 with RMS error

614 of 0.507 psu but only slightly with the value of AqGSFC being very similar at 0.515 psu. The

615 difference is in part due to a bias correction using climatological data was applied in the

616 computation of SmosBEC product.

617

618 It should be noted that there are significant differences even between the three Aquarius SSS

619 products. The differences are usually caused by different techniques in the retrieval of SSS.

620   Even when the retrieval techniques are the same such as those used in the AqGSFC and

621   AqNSIDC products, there are still biases associated with the geophysical filtering and smoothing

622   techniques. In addition, the masking of sea ice and land are different for the different products.

623   For example, inability to mask sea ice cover properly keeps the AqJPL data from capturing the

624   seasonal variability in SSS that is observed by AqGSFC and AqNSIDC products in the Arctic

625   region in the early autumn of 2014. Also, although SmosBEC provides SSS that is most

626   consistent with ship and CORA5.0 data, the masking of sea ice was not done properly in the

627   retrieval. This limit the usefulness of this (and also JPL) product in the Arctic basin and points to

628   the need to validate or improve the ice concentration product used to mask out sea ice

629   contaminated SSS.

630

631   Overall, all four products are highly correlated with CORA5.0 and ship data and the spatial and

632   temporal changes in distributions are consistent with changing surface salinity associated with

633   river run-off, sea ice and glacial melt and exchanges between the Arctic and the Pacific and

634   Atlantic Oceans. The products can therefore be used to gain understanding of changing

635   productivity in the region as may be associated with low salinity and phytoplankton blooms and

636   near the ice edges and changes in the circulation patterns of the ocean. The results also show

637   quantitatively that the Atlantic/Eastern side is consistently more saline than the Pacific/Western

638   side for all seasons which opens up some questions about differences in precipitation patterns and

639   mixing dynamics in the two oceans.

640

641   **Acknowledgements**

654

References

656   Aagard, K., and E.C., Carmack, J.H. Swift (1985), Thermohaline Circulation in the Arctic

657   Mediterranean Seas, *Journal of Geophysical Research,* Vol. 90, No. C3., pp. 4833-4846.

658   Banks, C. J., C. P. Gommenginger, M. A. Srokosz, H. M. Snaith (2012), Validating SMOS Ocean

659   Surface Salinity in the Atlantic with Argo and Operational Ocean Model Data, *IEEE*

660   *Transactions on Geoscience and Remote Sensing*, 50. pp.1688-1702, doi:

661   10.1109/tgrs.2011.2167340.

662   Berger M., A. Camps, J. Font, Y. Kerr, J. Miller, J. Johannessen, J. Boutin, M. R. Drinkwater, N.

663   Skou, N. Floury, M. Rast, H. Rebhan, and E. Attema, (August 2002), *Measuring Ocean*

664   *Salinity with ESA's SMOS Mission – Advancing the Science,* ESA Bulletin 111.

665 Boutin, J., N. Martin, G. Reverdin, X. Yin, and F. Gaillard (2013), Sea surface freshening inferred

666   from SMOS and ARGO salinity: impact of rain, *Ocean Science*. 9. pp. 183-192, doi:

667   10.5194/os-9-183-2013.

668 Boyer, T.P., J. I. Antonov, O. K. Baranova, H. E. Garcia, D. R. Johnson, R. A. Locarnini, A. V.

669   Mishonov, D. Seidov, I. V. Smolyar, and M. M. Zweng (2009), *World Ocean Database*

670   *2009, Chapter 1: Introduction, NOAA Atlas NESDIS 66*, Ed. S. Levitus, U.S. Gov.

671   Printing Office, Wash., D.C., 216 pp.

672 Broecker, W. S. (1997), Thermohaline circulation, the Achilles heel of our climate system: Will

673   man-made CO2 upset the current balance?, Science, 278, 1582-1588.

674 Brucker, L., E. P. Dinnat, and L. S. Koenig (2014), Weekly gridded Aquarius L-band

675   radiometer/scatterometer observations and salinity retrievals over the polar regions – Part

676   1: Product description, *The Cryosphere*, 8, pp. 905-913.

677 Brucker, L., E. P. Dinnat, and L. S. Koenig (2014), Weekly gridded Aquarius L-band

678   radiometer/scatterometer observations and salinity retrievals over the polar regions – Part

679   2: Initial product analysis, *The Cryosphere*, 8, pp. 915-930.

680 Cabanes, C., A. Grouazel, K. von Schuckmann, M. Hamon, V. Turpin, C. Coatanoan, F. Paris, S.

681   Guinehut, C. Boone, N. Ferry, C. de Boyer Montégut, T. Carval, G. Reverdin, S.

682   Pouliquen, and P. Y. Le Traon (2013), The CORA dataset: validation and diagnostics of

683   in-situ ocean temperature and salinity measurements. *Ocean Science,* 9, 1-18,

684   http://www.oceansci.net/9/1/2013/os-9-1-2013.html, doi:10.5194/os-9-1-2013

685 Cavalieri, D. J. and C.L. Parkinson (2012), Arctic sea ice variability and trends, 1979–2010, *The*

686   *Cryosphere*, 6, 881-889, doi:10.5194/tc-6-881-2012.

687 Chassignet, E.P., H.E. Hurlburt, O.M. Smedstad, G.R. Halliwell, P.J. Hogan, A.J. Wallcraft, R.

688   Baraille, R. Bleck (March 2007), The HYCOM (HYbrid Coordinate Ocean Model) data

689   assimilative system, *Journal of Marine Systems*, vol. 65, Issues 1–4, pp. 60-83,

690   Coachman, L.K. and C.A. Barnes. (1961) The Contribution of Bering Sea Water to the Arctic

691   Ocean. *Arctic,* Vol.14, No. 3. DOI: 10.14430/arctic3670

692

693   Comiso, J.C., R.A. Gersten, L.V. Stock, J. Turner, G.J. Perez, and K. Cho (2017), Positive Trend

694   in the Antarctic Sea Ice Cover and Associated Changes in Surface Temperature. *J.*

695   *Climate,* 30, 2251–2267, doi: 10.1175/JCLI-D-16-0408.1.

696   Comiso, J. C., C. L. Parkinson, R. Gersten, and L. Stock (2008), Accelerated decline in the Arctic

697   sea ice cover, *Geophys. Res. Lett*., 35, L01703, doi:10.1029/2007GL031972.

698   Gabarro C., E. Olmedo, A. Turiel, J. Ballabrera-Poy, J. Martinez, M. Portabella (2016), SMOS

699   sea surface salinity maps of the Arctic Ocean, *EGU General Assembly 2016,* Geophysical

700   Research Abstracts Vol. 18, EGU2016-7359-3

701   Dinnat, E. P., and D. M. Le Vine (2008), Impact of sun glint on salinity remote sensing: An

702   example with the Aquarius radiometer*, IEEE Trans. Geosci. Remote Sens.,* 46(10), 3137–

703   3150, doi:10.1109/TGRS.2008.2000629.

704   Dinnat, E. P., S. Abraham, D. M. Le Vine, P. De Matthaeis, and D. Jacob (2009), Effect of

705   emission from the moon on remote sensing of sea surface salinity: An example with the

706   Aquarius radiometer, *IEEE Geosci. Remote Sens. Lett.,* 6(2), 239–243,

707   doi:10.1109/LGRS.2008.2008822.

708   Dinnat, E., L. Brucker (2017), Improved Sea Ice Fraction Characterization for L-band

709   Observations by the Aquarius Radiometers, *IEEE Transactions on Geoscience and*

710   *Remote Sensing,* 0196-2892

711   Dinnat, E., L. Brucker, I. C. Alvarez (2014a), Assessment of the Aquarius Space-borne Sea

712   Surface Salinity Retrievals in Polar Oceans, *American Geophysical Union, Fall Meeting*

713   *2014*, Abstract #OS41C-1218.

714   Dinnat, E., J. Boutin, X. Yin, and D. Le Vine (2014b), Inter-comparison of SMOS and Aquarius

715   sea surface salinity: Effects of the dielectric constant and vicarious calibration. *In:*

716   *Microwave Radiometry and Remote Sensing of the Environment (MicroRad), 13th*

717   *Specialist Meeting*; pp. 55-60. doi: 10.1109/MicroRad.2014.6878907.

718   Dukhovskoy, D. S., et al. (2016), Greenland freshwater pathways in the sub-Arctic Seas from

719   model experiments with passive tracers, J. Geophys. Res. Oceans, 121, 877–907,

720   doi:10.1002/2015JC011290.

721   Durack, P. J., S. E. Wijffels, and R. J. Matear (2012), Ocean salinities reveal strong global water

722   cycle intensification during 1950 to 2000, *Science 336*, pp. 445-458.

723   Ebuchi, N., and H. Abe (2014), Evaluation of sea surface salinity observed by Aquarius, 2014

724   *IEEE Geoscience and Remote Sensing Symposium*, Quebec City, QC, pp. 4427-4430. doi:

725   10.1109/IGARSS.2014.6947473.

726   Gordon, A.L., and C.F. Giulivi. (2008) Sea Surface Salinity Trends: Over Fifty Years Within the

727   Subtropical North Atlantic, *Oceanography,* Vol. 21, No.1. pp. 21-29, March 2008.

728   Houssais, M.N., C. Herbaut, P. Schlichtholz, C. Rousset. (2007) Arctic Salinity Anomalies and

729   their Link to the North Atlantic during a Positive Phase of the Arctic Oscillation.

730   *ScienceDirect, Progress in Oceanography,* 73 (2007) 160-189. DOI:

731   10.1016/j.pocean.2007.02.005

732   Khan, S. A., et al. (2014), Sustained mass loss of the northeast Greenland ice sheet triggered by

733   regional warming, *Nat. Clim. Change*, **4**(4), 292–299, doi:10.1038/nclimate2161.

734   Kerr, Y., Waldteufel, J. P., Boutin, M. J. Escorihuela, J. Font, N. Reul, ... S. Mecklenburg (2010),

735   The SMOS mission: New tool for monitoring key elements of the global water cycle,

736   *Proceedings of the IEEE,* 98 (5), pp. 666-687.

737   Klein, L.A. and C. T. Swift (1977), An improved model for the dielectric constant of seawater at

738   microwave frequencies, *IEEE Transactions on Antennas and Propagation*, vol. AP-25, no.

739   1, pp. 104–111.

740   Kohler J., M. S. Martins, N. Serra, D. Stammer (2014), Quality Assessment of spaceborne sea

741   surface salinity observations over the northern North Atlantic, *Journal of Geophysical*

742   *Research: Oceans,* 120, pp. 94-112. doi: 10.1002/2014JC010067.

743   Kubryakov, A., S. Stanichny, and A. Zatsepin (2016), River plume dynamics in the Kara Sea

744   from altimetry-based lagrangian model, satellite salinity and chlorophyll data, *Remote*

745   *Sens. Environ.,* 176, 177–187, doi:10.1016/j.rse.2016.01.020.

746   Lagerloef, G., F. R. Colomb, D. L. Vine, F. Wentz, S. Yueh, C. Ruf, ... C. Swift (2008), The

747   Aquarius/SAC-D mission: Designed to meet the salinity remote-sensing challenge,

748   *Oceanography*, 21(1), pp. 68-81.

749   Lagerloef, G., H. Y. Kao, T. Meissner, J. Vazquez (2015), *Aquarius Salinity Validation Analysis;*

750   *Data Version 4.0. 2*. Available online at ftp://podaac-ftp.jpl.nasa.gov. Accessed: 26 Aug

751   2016.

752   Lagerloef, G., Kao, H.Y., Meln, O., Hacker, P., Hackert, E., Chao, Y., Hilburn, K., Meissner, T.,

753   Yueh, S., Hong, L., and Lee, T. (2013*), Aquarius Validation Analysis Technical Report,*

754   AQ-041-PS-0016, NASA, Pasadena, CA, USA.

755 Lehner, F., C. C. Raible, D. Hofer, and T. F. Stocker (2012), The freshwater balance of polar

756   regions in transient simulations from 1500 to 2100 AD using a comprehensive coupled

757   climate model, *Clim. Dyn.*, **39**(1-2), 347–363, doi:<u>10.1007/s00382-011-1199-6</u>.

758 Le Vine, D., G. Lagerloef, and S. Torrusio (2010), Aquarius and remote sensing of sea surface

759   salinity from space, *Proc. IEEE*, 98(5), 688–703.

760 Le Vine, D. M., E. P. Dinnat, S. Abraham, P. De Matthaeis, and F. J. Wentz (2011), The Aquarius

761   simulator and cold-sky calibration*, IEEE Trans. Geosci. Remote Sens*., 49(9), 3198–3210,

762   doi:10.1109/TGRS.2011.2161481.

763 Le Vine, D. M., S. Abraham, C. Utku, and E. P. Dinnat (2013), Aquarius third stokes parameter

764   measurements: Initial results*, IEEE Geosci. Remote Sens. Lett.,* 10(3), 520–524,

765   doi:10.1109/LGRS.2012.2211994.

766 Lilly, J.M., and G. S. Lagerloef (January, 2008), *Aquarius Level 3 Processing Algorithm*

767   *Theoretical Basis Document Version 0.9.* Available online at ftp://podaac-ftp.jpl.nasa.gov.

768   Accessed: 26 Aug 2016.

769 Martin, A. C. H., J. Boutin, D. Hauser, and E. P. Dinnat (2014), Active-passive synergy for

770   interpreting ocean L-band emissivity: Results from the CAROLS airborne campaigns, *J.*

771   *Geophys. Res. Ocean.,* 119(8), 4940–4957, doi:10.1002/2014JC009890.

772 Mecklenburg, S., Drusch, M., Kerr, Y., Font, J., Martin-Niera, M., Delwart, S., ... Crapoicchio, R.

773   (2012), ESA's soil moisture and ocean salinity mission: Mission performance and

774   operations, *IEEE Transactions on Geoscience and Remote Sensing*, 50 (5), pp. 1354-1366.

775 Meissner, T., Wentz, F.J., and Scott, J. (2015), *Remote Sensing Systems SMAP [8day] Mean Sea*

776   *Surface Salinity on 0.25 deg grid, Version 1.0. (BETA).* Remote Sensing Systems, Santa

777   Rosa, CA., Available online at www.remss.com/missions/smap. Accessed: 16 Sept 2016.

778   Meissner, T. and Wentz, F. (2012), The emissivity of the ocean surface between 6 and 90 GHz

779   over a large range of wind speeds and earth incidence angles, *IEEE Trans. Geosci. Remote*

780   *Sensing,* vol. 50, no. 8, pp. 3004– 3026.

781   Meissner, T., F. J. Wentz, and L. Ricciardulli (2014), The emission and scattering of L-band

782   microwave radiation from rough ocean surfaces and wind speed measurements from the

783   Aquarius sensor*, J. Geophys. Res. Ocean*., 119(9), 6499–6522,

784   doi:10.1002/2014JC009837.

785   Meissner, T., Wentz, F.J., and De Mattheis P. (July 15, 2015), *Addendum IV to ATBD, Remote*

786   *Sensing Systems Report #071515*, Santa Rosa, CA., Available online at ftp://podaac-

787   ftp.jpl.nasa.gov/allData/aquarius/docs/v4/AQ-014-PS-

788   0017_AquariusATBD_Level2_Addendum4_DatasetVersion4.0.pdf. Accessed: 26 August

789   2016.

790   Melnichenko, O., Hacker, P., Maximenko, N., Lagerloef, G., and Potemra, J. (2014), Spatial

791   Optimal Interpolation of Aquarius Sea Surface Salinity: Algorithms and Implementation

792   in the North Atlantic, *Journal of Atmospheric and Oceanic Technology*, 31, pp. 1583-

793   1600.

794   Nichols, J.E. and V. Vohra (2004), *Noise over water surfaces in Landsat TM images*,

795   International Journal of Remote Sensing, 25 (11), pp. 2087 - 2093.

796   Nummelin, A., M. Ilicak, C. Li, and L. H. Smedsrud (2016), Consequences of future increased

797   Arctic runoff on Arctic Ocean stratification, circulation, and sea ice cover, J. Geophys.

798   Res. Oceans, 121, 617–637, doi:10.1002/2015JC011156.

799   Rudels, B., (2011) Volume and freshwater transports through the Canadian Arcgtic Archipelago-

800   Baffin Bay system, J. Geophys. Res, 116, C00D10, doi:10.1029/2011JC007019.

36

801   Schmitt, R.W. (March 2008), Salinity and the Global Water Cycle, *Oceanography,* 21 (1). 12-19.

802   Serreze, M.C., Barrett, A.P., Slater, A.G., Woodgate, R.A., Aagaard, K., Lammers, R.B., Steele,

803   M., Moritz, R., Meredith, M., and Lee, C.M. (2006), The large-scale freshwater cylce of

804   the Arctic, *Journal of Geophysical Research*, 111, C11010. doi: 10.1029/2005JC003424.

805   Szekely, T., Gourrion, J., Brion, E., Von Schuckmann, K. Reverdin, G., Grouazel, A., and

806   Pouliquel, S., 2015: CORA4.1: A delayed-time validated temperature and salinity profiles

807   and timeseries product. Proceeding from 7e EuroGOOS conference, To be published.

808   Vaughan, D., J. Comiso, I.,Allison, J.Carrasco, G.Kaser, R.Kwok, P.Mote, T.Murray, F.Paul,

809   J.Ren, E.Rignot, O.Solomina, K.Steffen, and T.Zhang (2013), *Observations: Cryosphere,*

810   *in: Climate Change 2013: The Physical Science Basis. Contribution of Working Group I*

811   *to the Fifth Assessment Report of the Intergovernmental Panel on Climate Change*, edited

812   by: Stocker, T., Qin, D., Plattner, G.-K., Tignor, M., Allen, S., Boschung, J., Nauels, A.,

813   Xia, Y., Bex, V., and Midgley, P., Cambridge University Press, New York, NY, USA,

814   2014.

815   Wentz, F. J., and D. M. LeVine (2012), *Aquarius salinity retrieval algorithm version 2: Algorithm*

816   *theoretical basis document,* RSS Tech. Rep. 082912, pp. 45. Available at ftp://podaac-

817   ftp.jpl.nasa.gov/allData/aquarius/docs/v2/AQ-014-PS-0017_AquariusATBD_Level2. pdf.

818   Accessed: 26 August 2016.

819   Wentz, F.J., and S. H. Yueh (August 16, 2011), *Algorithm Theoretical Basis Document (ATBD),*

820   *Version 1*, Aquarius Salinity Retrieval Algorithm, RSS Tech Report 081611. Accessed: 26

821   August 2016.

822   Yueh, S. H., and J. Chaubell (2012), Sea Surface Salinity and Wind Retrieval Using Combined

823   Passive and Active L-Band Microwave Observations, *Geosci. Remote Sensing, IEEE*

824   *Trans.,* 50(4), 1022–1032, doi:10.1109/TGRS.2011.2165075.

825   Yueh, S. H., R. West, W. J. Wilson, F. K. Li, E. G. Njoku, and Y. Rahmat-Samii (2001), Error

826   sources and feasibility for microwave remote sensing of ocean surface salinity, *IEEE*

827   *Trans. Geosci. Remote Sens.*, 39(5), 1049–1060.

828   Yueh, S.H., S. J. Dinardo, G. Gore, and F. K. Li (2010), Passive and Active L-Band Microwave

829   Observations and Modeling of Ocean Surface Winds, *IEEE Transactions on Geoscience*

830   *and Remote Sensing,* 48(8), 3087-3100.

831   Yueh, S.H., W. Tang, A. Fore, and A. Hayashi (September 20, 2015), *Aquarius CAP Algorithm*

832   *and Data User Guide version 4.0*, Available online at ftp://podaac-

833   ftp.jpl.nasa.gov/allData/aquarius/docs/CAPv2/Aquarius-CAP-User-Guide-v2.0.pdf

834   Accessed: 26 August 2016.

835   Yueh S.H., W. Tang, A. Fore, A. Hayashi, Y.T. Song, and G. Lagerloef (2014), Aquarius

836   geophysical model function and combined active passive algorithm, for ocean surface

837   salinity and wind retrieval, *Journal of Geophysical Research: Oceans*, 119, 5360-5379.

838   doi:10.1002/2014JC009939.

839

840

841

842

843

844

845   **Table 1.** Comparison of space observed SSS products and Polarstern TSG measurements with the

846   values averaged over all collocated measurements for 2012 and 2014. (SmosBEC product

847   available only from 2011-2013).

	15 Jun - 06 Oct 2012				08 Jun – 04 Oct 2014		
	AqGSFC	AqJPL	AqNSIDC	SmosBEC	AqGSFC	AqJPL	AqNSIDC
Correlation	0.974	0.964	0.972	0.959	0.876	0.393	0.780
SD	0.467	0.547	0.524	0.486	0.569	0.408	0.691
Bias	0.117	-0.170	0.263	0.011	0.572	0.663	-0.555
RMSE	0.515	0.585	0.686	0.507	0.806	0.838	0.886

848

849   **List of Captions:**

850   **Figure 1.** Panel a shows location of in situ data from the CORA v5.0 for year 2012 as received

851   by the Coriolis data Centre and illustrates the paucity of data in the Arctic region. Blue data points

852   represent Argo data while the red points are from other sources (e.g., XBT, CTD, ship etc.). Also

853   indicated are various seas in the region as well as the mouth of key rivers. Panels b-c illustrate

854   dependence of T_B in the V and H polarizations to SST at different SSS ranging from 25-29 psu at

855   1.43 GHz frequency and 35° incidence angle.

856   **Figure 2**. Aquarius Level-2 SSS three beams (dotted line: Beam1-black; Beam2-red; Beam3-

857   blue) passing through North Atlantic (Ascending) and North Pacific (Descending) starting at

858   6:12PM UTC on July 2, 2012. Solid line show result after applying median filter along track with

859   window of 9 observations.

860   **Figure 3.** Polarstern track from (a) 15 June – 06 October 2012 and (b) 08 June – 04 October

861   2014, covering Norwegian Sea, Greenland Sea, Fram Strait, Arctic Ocean, Barents Sea and

862   Laptev Sea. Letters A-D in 2012 and E-G in 2014 are portions of the ship's tracks used for the

863   validation of the satellite derived salinity measurements. Tick marks of varied shapes indicate

864   extent of each segment used.

865   **Figure 4.** Comparison of Polarstern TSG measurements (black) versus collocated satellite-

866   derived SSS products namely: AqGSFC (red), AqJPL (orange), AqNSIDC (blue), and SmosBEC

867   (green) from 15 June – 06 October 2012. Areas (a-d) are segments of the ship tracks that are not

868   contaminated by sea ice or land as illustrated in Figure 3. Scatter plots of co-located (a) AqGSFC;

869   (b) AqJPL; (c) AqNSIDC; and (d) SmosBEC versus Polarstern TSG measurements for the same

870   period.

871   **Figure 5.** Comparison of Polarstern TSG measurements (black) versus collocated satellite-

872   derived SSS measurements from AqGSFC (red), AqJPL (orange), AqNSIDC (blue), and

873   SmosBEC (green) from 08 June – 04 October 2014**.** Areas (a-d) were highlighted due to the

874   absence of possible contamination from sea ice and land. Scatter plots of co-located (a)

875   AqGSFC; (b) AqJPL; and (c) AqNSIDC versus Polarstern TSG measurements for the same

876   period.

877   **Figure 6.** In situ SSS map from 26 August 2011 to 06 June 2015 using (a) CORA5.0 and scatter

878   plots of collocated satellite-derived SSS data from (b) AqGSFC, (c) AqJPL, (d) AqNSIDC, and

879   (e) SmosBEC versus CORA5.0. Scatterplots of each of the products with CORA5.0 are shown in

880   blue while data points common among all the products with CORA5.0 are shown in red.

881   **Figure 7.** Difference map (e) shows the difference between processed (a) AqGSFC from

882   (b) AqJPL; difference map (f) is the difference between (a) AqGSFC and (c) AqNSIDC;

883   difference map (g) between (a) AqGSFC and (d) SmosBEC; and difference map (h) is the

884   between (b) AqJPL and (d) SmosBEC all in the middle of spring of 2012.

885   **Figure 8.** Difference map (e) shows the difference between processed (a) AqGSFC from (b)

886   AqJPL (b); difference map (f) is the difference between (a) AqGSFC and (c) AqNSIDC ;

887   difference map (g) between (a) AqGSFC and (d) SmosBEC; and difference map (h) is the

888   between (b) AqJPL and (d) SmosBEC all in the end of early autumn of 2012.

889   **Figure 9.** Inter-annual SSS distribution in spring of 2011-2015 from (a) AqGSFC, (b) AqJPL, (c)

890   AqNSIDC and (d) SmosBEC product from 2012-2013. Also shown are 33 psu contours in black.

891   **Figure 10.** Inter-annual SSS distribution in early autumn 2011-2014 from (a) AqGSFC, (b)

892   AqJPL, (c) AqNSIDC and (d) SmosBEC product from 2011-2013. Also shown are 33 psu

893   contours in black.

894   **Figure 11.** Monthly SSS averages of AqGSFC (red), AqJPL (yellow), AqNSIDC (blue) from

895   August 2011 to June 2015 and SmosBEC from August 2011 to December 2013 in the (a) Pacific

896   Ocean (> 50°N, < 65°N, < 270°E, > 90°E), Atlantic Ocean (> 50°N, < 65°N, < 90°E, > 270°E),

897   Western Arctic Basin (> 65°N, < 180°E, > 0°E), and Eastern Arctic Basin (> 65°N, > 180°W, >

898   0°W). SB2 sea ice concentration monthly averages plotted on c-d are shown as the gray dashed

899   line.

900

901

902

Figure 1. Panel a shows location of in situ data from the CORA v5.0 for year 2012 as received
by the Coriolis data Centre and illustrates the paucity of data in the Arctic region. Blue data points
represent Argo data while the red points are from other sources (e.g., XBT, CTD, ship etc.). Also
indicated are various seas in the region as well as the mouth of key rivers. Panels b-c illustrate
dependence of T_B in the V and H polarizations to SST at different SSS ranging from 25-29 psu at
1.43 GHz frequency and 35° incidence angle.

909
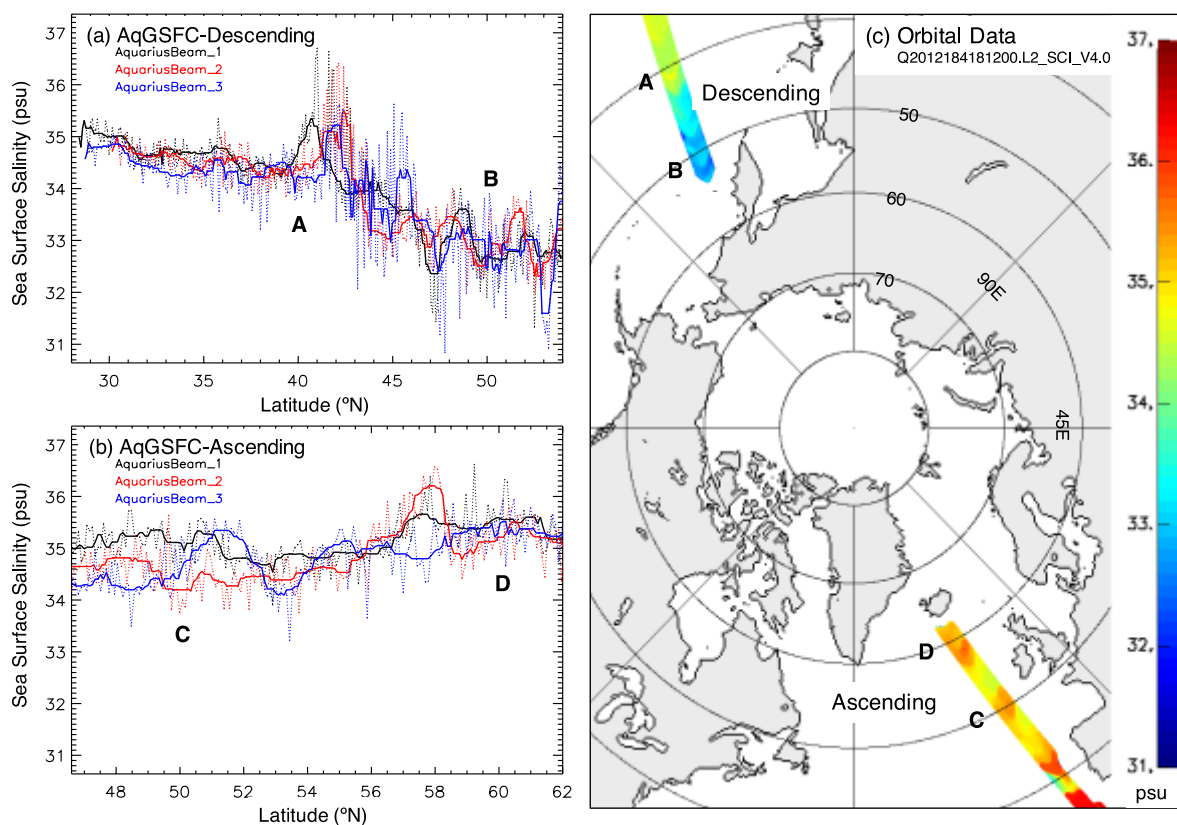
Figure 2. Aquarius Level-2 SSS three beams (dotted line: Beam1-black; Beam2-red; Beam3-

blue) passing through North Atlantic (Ascending) and North Pacific (Descending) starting at

6:12PM UTC on July 2, 2012. Solid line show result after applying median filter along track with

window of 9 observations.

Figure 3. Polarstern track from (a) 15 June – 06 October 2012 and (b) 08 June – 04 October

2014, covering Norwegian Sea, Greenland Sea, Fram Strait, Arctic Ocean, Barents Sea and

Laptev Sea. Letters A-D in 2012 and E-G in 2014 are portions of the ship's tracks used for the

validation of the satellite derived salinity measurements. Tick marks of varied shapes indicate
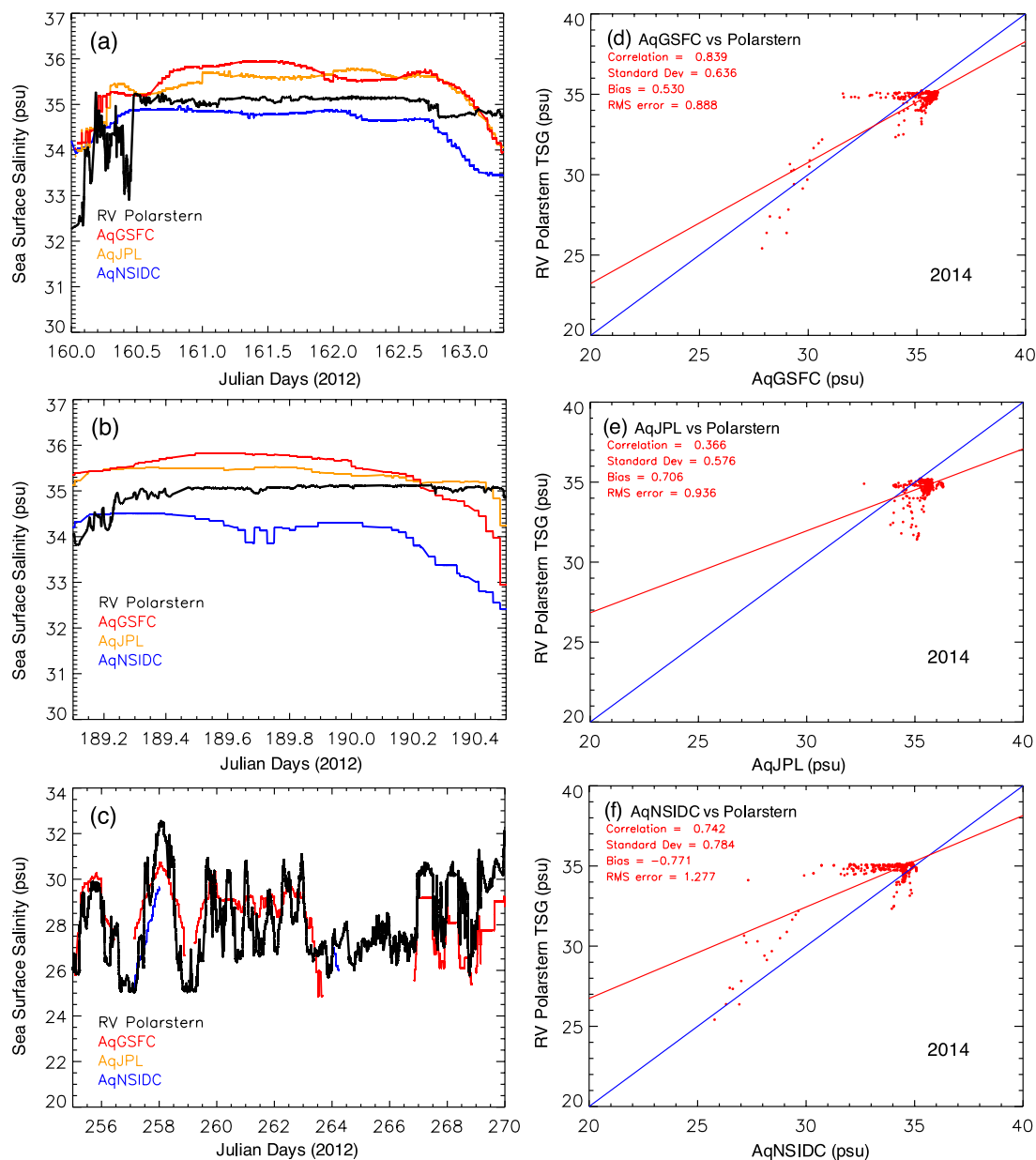
extent of each segment used.
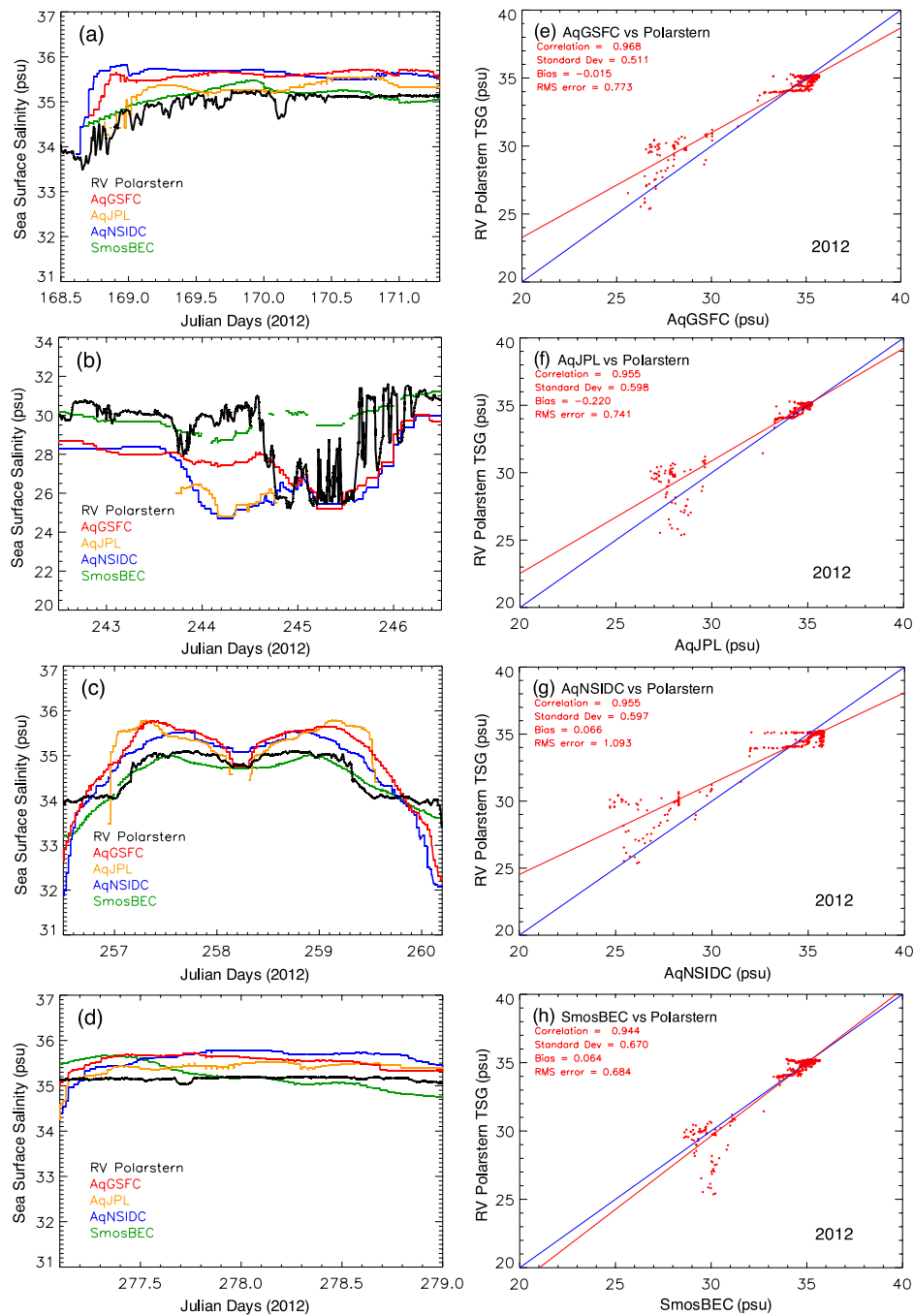
919

920

Figure 4. Comparison of Polarstern TSG measurements (black) versus collocated satellite-derived SSS products namely: AqGSFC (red), AqJPL (orange), AqNSIDC (blue), and SmosBEC (green) from 15 June – 06 October 2012. Areas (a-d) are segments of the ship tracks that are not

924   contaminated by sea ice or land as illustrated in Figure 3. Scatter plots of co-located (a) AqGSFC;

925   (b) AqJPL; (c) AqNSIDC; and (d) SmosBEC versus Polarstern TSG measurements for the same

926   period.

927

928

Figure 5. Comparison of Polarstern TSG measurements (black) versus collocated satellite-derived SSS measurements from AqGSFC (red), AqJPL (orange), AqNSIDC (blue), and SmosBEC (green) from 08 June – 04 October 2014**.** Areas (a-d) were highlighted due to the absence of possible contamination from sea ice and land. Scatter plots of co-located (a) AqGSFC; (b) AqJPL; and (c) AqNSIDC versus Polarstern TSG measurements for the same period.
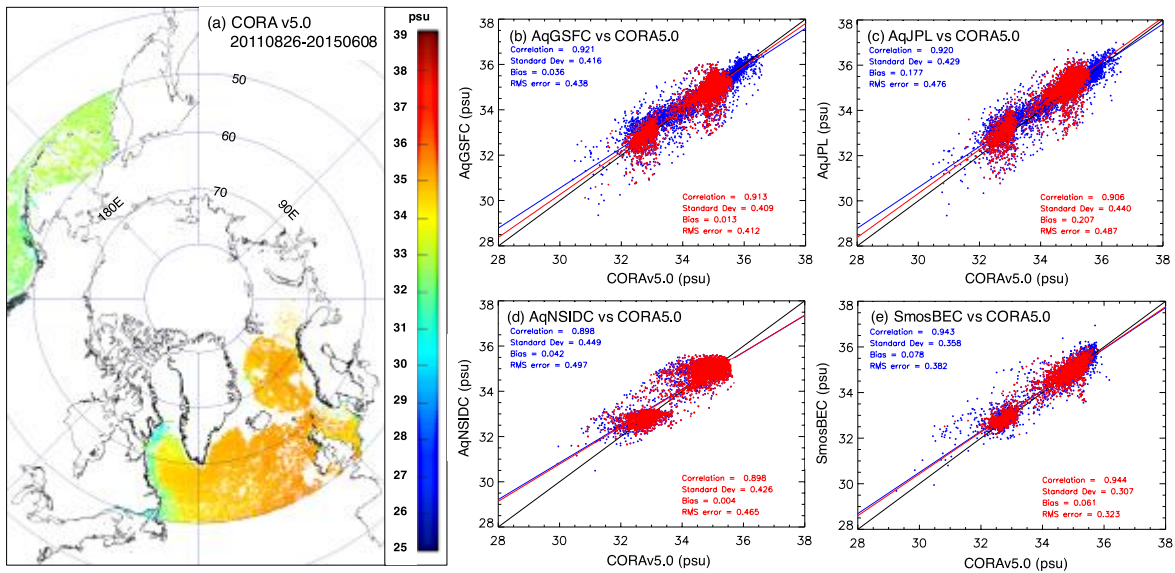
Figure 6. In situ SSS map from 26 August 2011 to 06 June 2015 using (a) CORA5.0 and scatter plots of collocated satellite-derived SSS data from (b) AqGSFC, (c) AqJPL, (d) AqNSIDC, and (e) SmosBEC versus CORA5.0. Scatterplots of each of the products with CORA5.0 are shown in blue while data points common among all the products with CORA5.0 are shown in red.
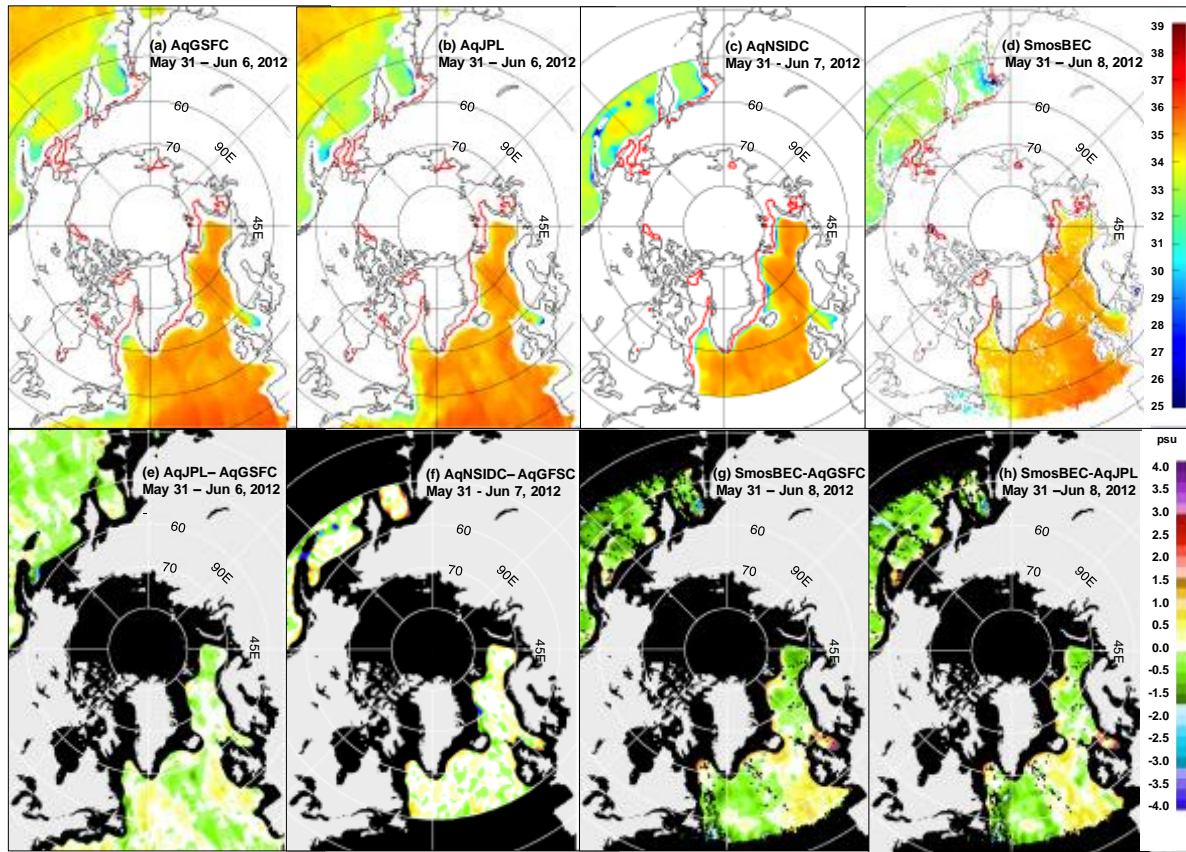
Figure 7. Difference map (e) shows the difference between processed (a) AqGSFC from

(b) AqJPL; difference map (f) is the difference between (a) AqGSFC and (c) AqNSIDC;

difference map (g) between (a) AqGSFC and (d) SmosBEC; and difference map (h) is the

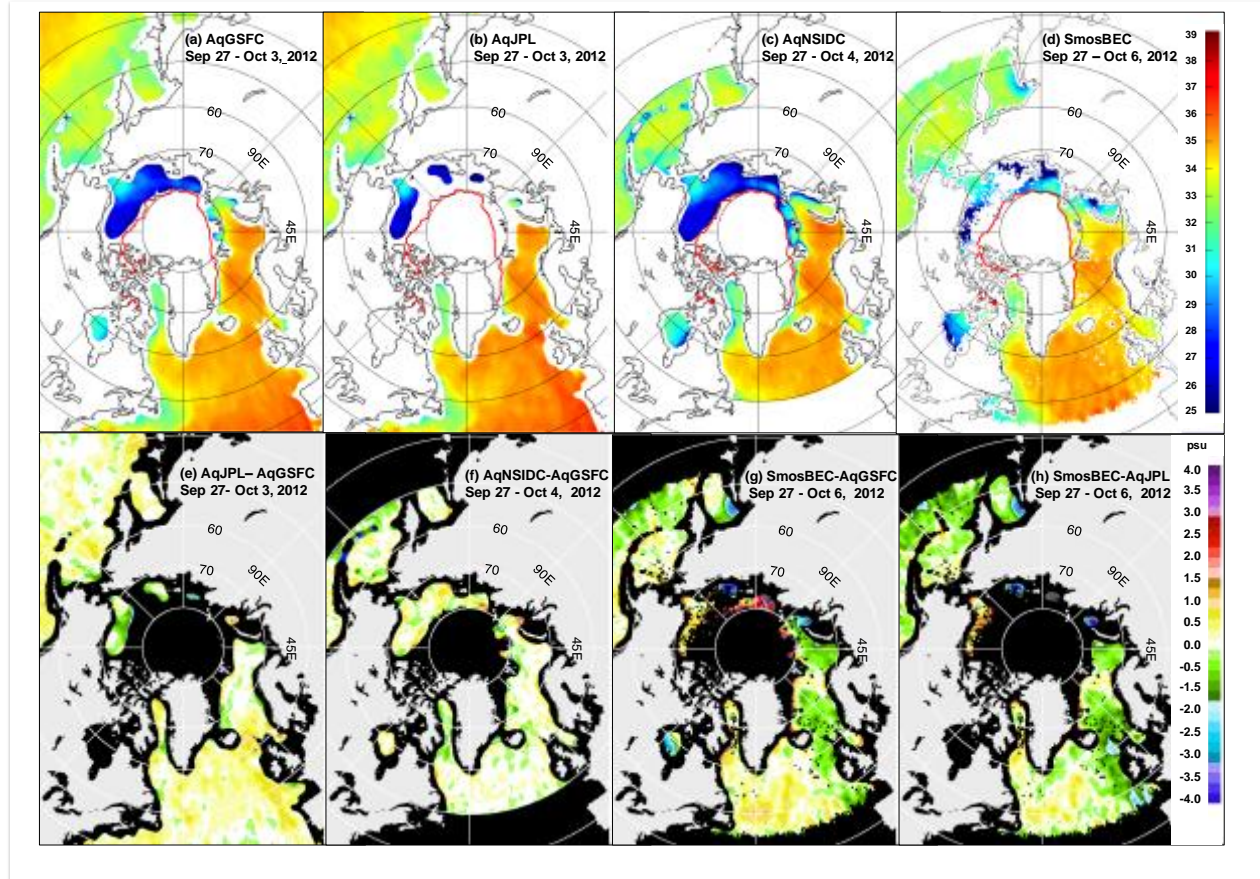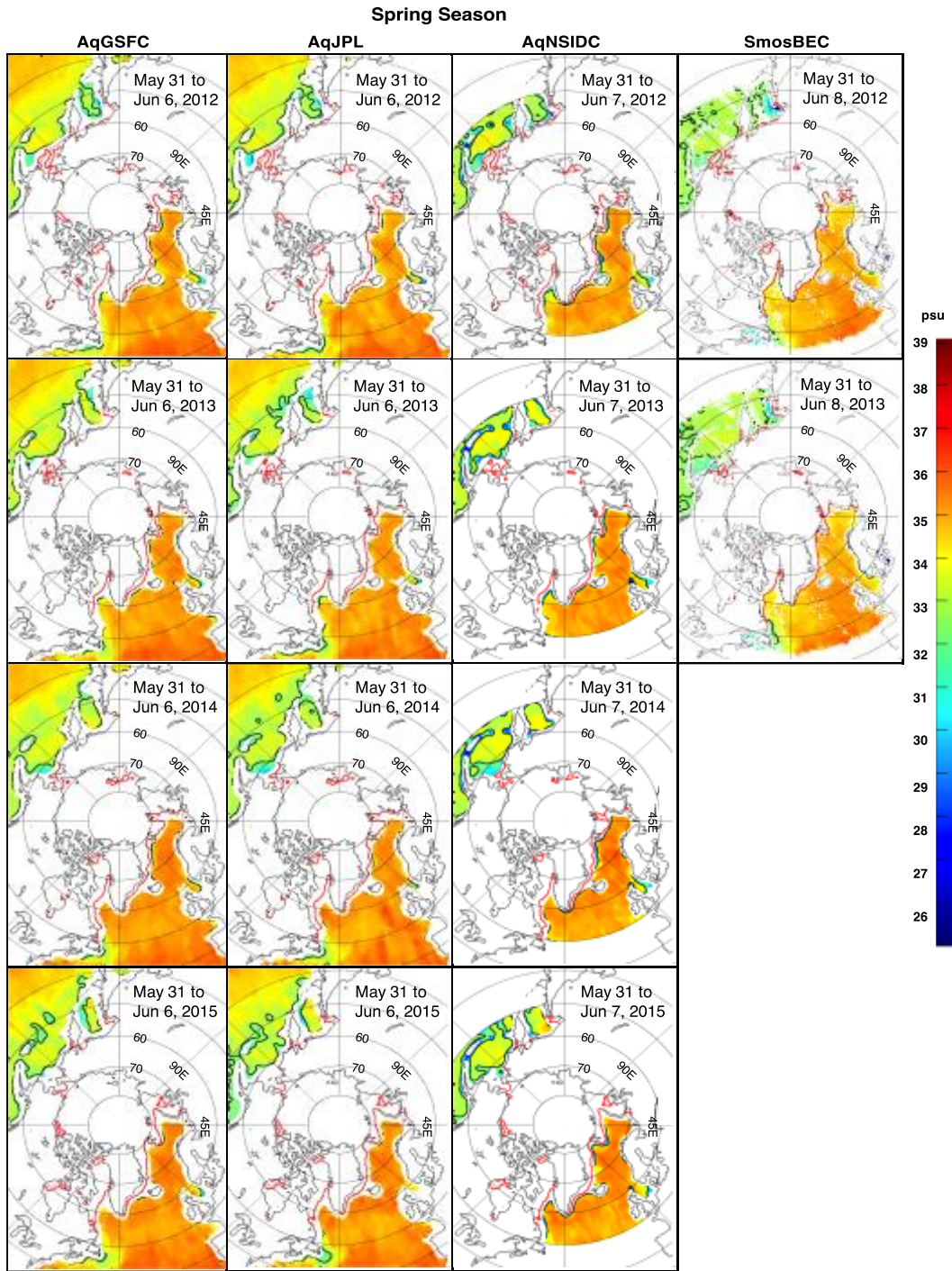between (b) AqJPL and (d) SmosBEC all in the middle of spring of 2012.

Figure 8. Difference map (e) shows the difference between processed (a) AqGSFC from (b)

AqJPL (b); difference map (f) is the difference between (a) AqGSFC and (c) AqNSIDC ;

difference map (g) between (a) AqGSFC and (d) SmosBEC; and difference map (h) is the

between (b) AqJPL and (d) SmosBEC all in the end of early autumn of 2012.

Figure 9. Inter-annual SSS distribution in spring of 2011-2015 from (a) AqGSFC, (b) AqJPL, (c) AqNSIDC and (d) SmosBEC product from 2012-2013. Also shown are 33 psu contours in black.
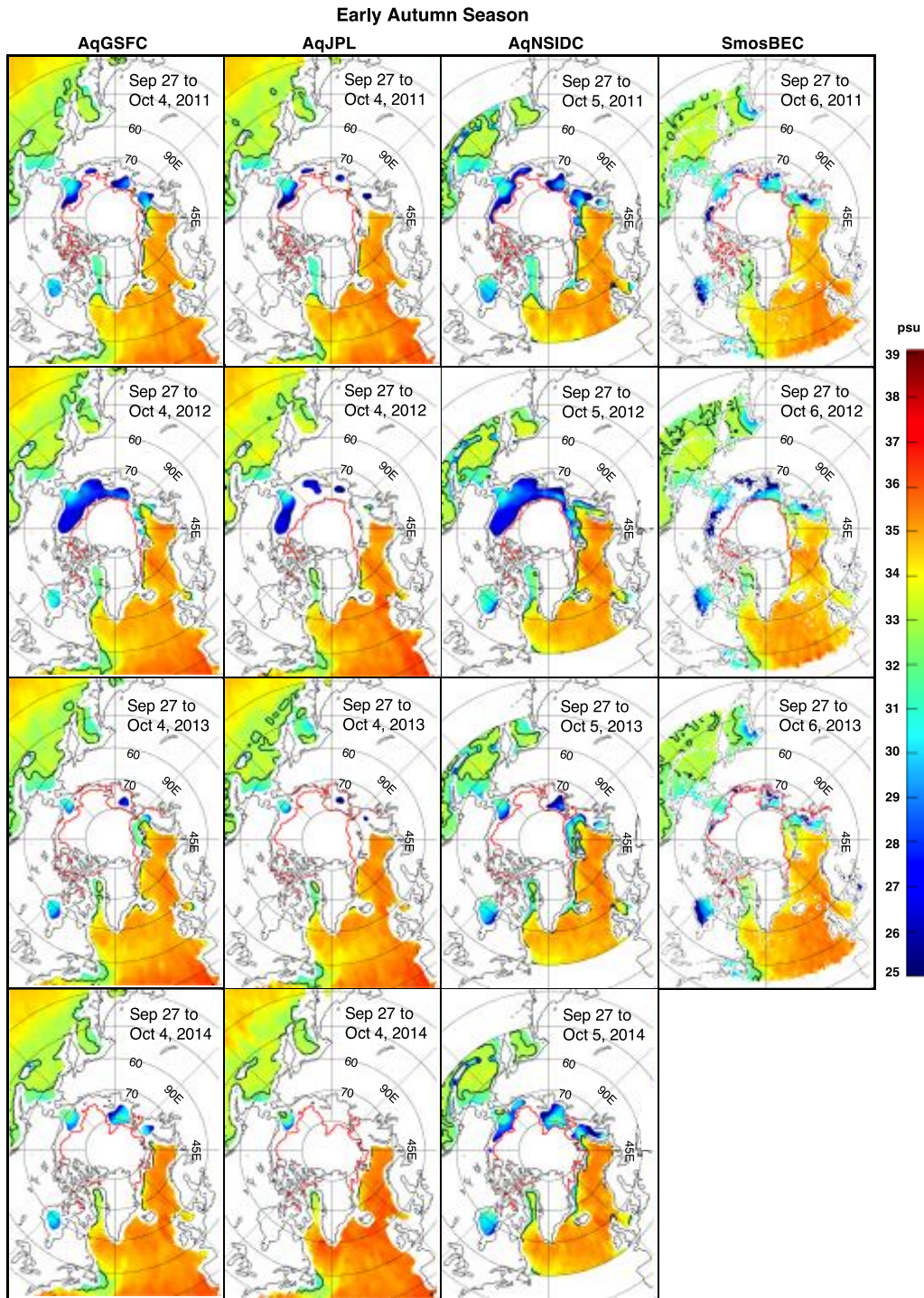
956

Figure 10. Inter-annual SSS distribution in early autumn 2011-2014 from (a) AqGSFC, (b)

AqJPL, (c) AqNSIDC and (d) SmosBEC product from 2011-2013. Also shown are 33 psu
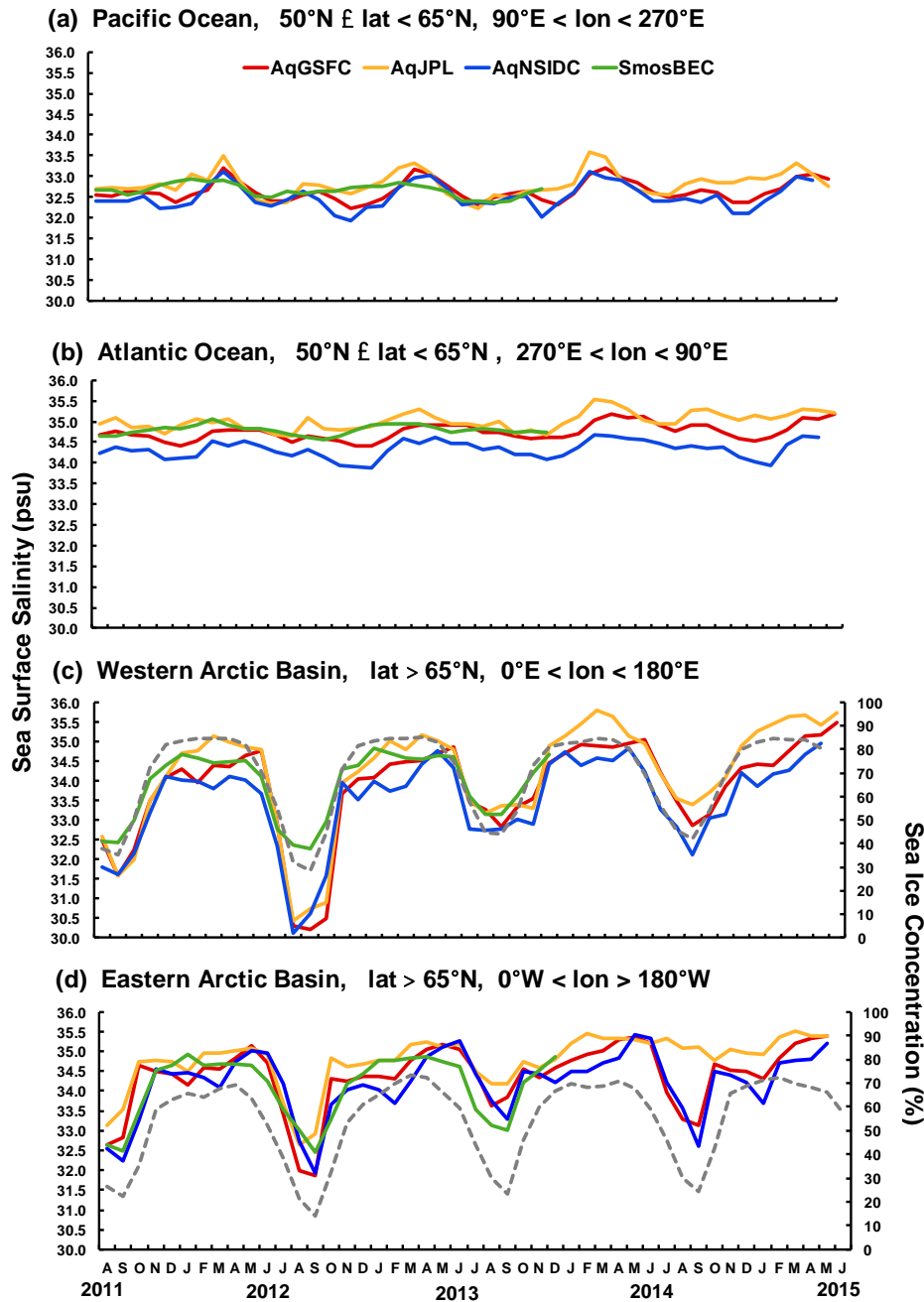
contours in black.

(a) Pacific Ocean, 50°N £ lat < 65°N, 90°E < lon < 270°E

(b) Atlantic Ocean, 50°N £ lat < 65°N , 270°E < lon < 90°E

(c) Western Arctic Basin, lat > 65°N, 0°E < lon < 180°E

(d) Eastern Arctic Basin, lat > 65°N, 0°W < lon > 180°W

960

Figure 11. Monthly SSS averages of AqGSFC (red), AqJPL (yellow), AqNSIDC (blue) from

August 2011 to June 2015 and SmosBEC from August 2011 to December 2013 in the (a) Pacific

Ocean (> 50°N, < 65°N, < 270°E, > 90°E), Atlantic Ocean (> 50°N, < 65°N, < 90°E, > 270°E),

964   Western Arctic Basin (> 65°N, < 180°E, > 0°E), and Eastern Arctic Basin (> 65°N, > 180°W, >

965   0°W). SB2 sea ice concentration monthly averages plotted on c-d are shown as the gray dashed

966   line.